HYDRODYNAMIC MODELING OF MULTI-COMPONENT IONIZED GAS FLOW FOR DC AND RF DISCHARGES

A thesis submitted to

KETTERING UNIVERSITY

in partial fulfillment
of the requirements for the
degree of

MASTER OF SCIENCE IN MECHANICAL ENGINEERING

by

HARIBALAN KUMAR

September 2005

Author: Haribalan Kumar

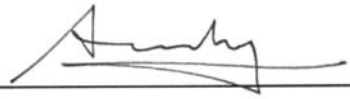

Faculty Advisor: Dr. Subrata Roy

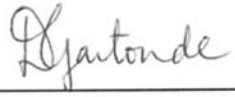

Committee Member: Dr. Datta Gaitonde

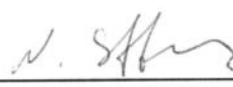

Committee Member: Dr. Natalia Sternberg

DISCLAIMER

This thesis is being submitted as partial and final fulfillment of the degree requirements of Kettering University needed to obtain a Master of Science in Mechanical Engineering Degree.

The conclusions and opinions expressed in this thesis are those of the writer and do not necessarily represent the position of Kettering University or any of its directors, officers, agents or employees with respect to the matters discussed.

PREFACE

This thesis represents the capstone of my work in the Department of Mechanical Engineering at Kettering University. I would like to express my sincere appreciation to Dr. Subrata Roy, who in the capacity of my faculty advisor, introduced me to the subject. His technical guidance and moral support has made this thesis possible. I would like to acknowledge and extend my sincere gratitude to the thesis committee members, Dr. Datta Gaitonde, Computational Sciences Branch, Air Vehicles Directorate and Dr. Natalia Sternberg, Professor of Mathematics and Computer Science, Clark University for their valuable time and guidance. I would like to acknowledge Dr. K. Joel Berry, Head of the Department of Mechanical Engineering for his genuine help and concern during the period of thesis writing.

I would like to thank my colleagues at the Computational Plasma Dynamics Laboratory (CPDL), Dr. Kunwar Pal Singh and Richard Anderson for their support in the past two years. I am also grateful to Arlene Hunt and Jodi Dorr from office of sponsored research, for their nurturing support during my stay at Kettering University. Finally I would like to acknowledge the faculty, staff and students of Kettering University who have knowingly or unknowingly helped me towards the successful completion of this thesis.

TABLE OF CONTENTS

LIST OF ILLUSTRATIONS

Figures **Page**

I. INTRODUCTION

Plasmas are conductive assemblage of photons, electrons, positive and negative ions and neutrals in isolated states exhibiting bulk effect. Plasmas find application in a wide spectrum of fields ranging from electric propulsion for spacecraft thrusters; fusion related high energy confinement systems to industrial applications like thin film deposition, etching, surface sterilization and material processing. Recently, the use of plasma as actuators has found tremendous interest for both low and high-speed aerodynamic flow control applications.

Plasma forms when electrical discharge is applied in a plasma source. Depending upon the frequency of the exciting field, discharges may be broadly classified as:

- Direct current (dc) discharge
- Pulsed dc discharge (Kilo Hertz)
- Radio-frequency (rf) discharge (Mega Hertz)
- Microwave discharge (Giga Hertz)
- Laser plasma (Pico Hertz)

This thesis is limited to dc and rf discharges.

In understanding the dynamics of plasma, electrons and ions are two important species that are generally investigated. Plasma resulting from single ionization of neutral gas generally contains equal number of these positive and negative charge carriers. In this situation, the oppositely charged particles are strongly attracted, and tend to electrically

neutralize one another on macroscopic length-scales. Such plasmas are termed quasi-neutral.

The thermal speed of electrons is much higher than that of ions due to the large difference in masses (of the order of 10^3 or higher). This is the reason why easy transfer of electrical energy from the power supply to the plasma electrons is plausible. The formation of sheath is a result of this simple property. The large m_i/m_e ratio allows the electrons to travel with much higher velocity in the plasma than the ions. When an object is placed in contact with the plasma, the much higher electron current to the object will preferentially removes electrons from the plasma in the vicinity of the object. This depletion of electrons leaves a space-charge region of ions, which sets up an electric field to further repel most of the electrons from leaving the plasma. Sheath, may hence be understood as a charge separated electrical boundary layer formed near an electrode. Sheath is also the distance over which electric fields shield mobile charge carriers (e.g. electrons) in plasmas and other conductors. It is quantified using the Debye length, λ_D , (named after the Dutch chemist) which is given by the expression,

$$\lambda_D = \sqrt{\frac{kT}{4\pi Ne^2}} \tag{1}$$

for a bulk density, N in m^{-3} and temperature, T in Kelvin. λ_D is the length scale over which significant charge separation can occur. In Equation 1, the inverse relation of Debye length (and hence sheath thickness) with number density may be observed.

Overview of Discharge Models

In trying to understand the dynamics of the system of plasma, Roy Choudhuri (1998) identifies levels of treatment for fluids and plasma. When number of particles to be studied is large making quantum description of particle unrealistic, a distribution is usually employed to describe its characteristics. A distribution function describes properties in a six-dimensional phase-space in terms of position and velocity coordinates. The treatment of this distribution function gives rise to varying approaches to describe processes behind a discharge. A kinetic approach tries to solve some of velocity distribution functions directly. For example, particle approaches like Particle In Cell (PIC) or Monte Carlo involves plasma characterization by following millions of computational particles for each species. The dynamics are followed using Newtonian equation. The disadvantage arises from using high-density systems when methods like PIC become prohibitively expensive. Fluid or hydrodynamic schemes are based on conservation laws derived from moments of Boltzmann equation. They are obtained by averaging over velocity coordinates of the distribution resulting in macroscopic quantities like number density, mean velocity etc. With proper choice of boundary conditions and accurate transport properties, they give reasonably accurate results in a much shorter time. Hybrid schemes combining fluid and kinetic approaches are also used, for example in stationary plasma (Hall) thruster modeling where ions are tracked using PIC while the electrons are simulated using fluid descriptions (Hagelaar et. al., 2002 and Fife, 1995).

Literature Review

There have been number of analytical and numerical attempts to understand discharge between parallel plates in one dimension under dc and rf conditions. Sternberg

and Godyak (1996) studied the plasma-sheath transition region of a bounded plasma discharge under dc conditions. The locations of the plasma and sheath boundaries are evaluated, as well as the ion velocity and the electric field at the boundary. A comparison of the separate plasma and the sheath solutions with the solution of the bounded plasma-wall problem has shown good agreement. They have also evaluated the position of the sheath edge and the value of the electric field at the sheath edge using asymptotic matching techniques (Sternberg and Godyak, 2003).

Roy et. al. (2003) developed a computationally efficient one-dimensional subgrid embedded finite element formulation for plasma-sheath dynamics. Kumar and Roy (2005) have elaborated this self-consistent finite element algorithm for two-fluid plasma and have investigated related numerical issues. The applications included dc and rf sheath inside a glow discharge tube with argon. Godyak and Sternberg (1990) have modeled the dynamics of a symmetric rf discharge sheath in the frequency range $\omega_{pi} << \omega_{rf} << \omega_{pe}$ for varying degrees of collision and sheath voltages. Analytical expressions for sheath characteristics have been derived based on conditions employed at plasma boundary treating sheath and plasma separately. Slemrod (2003) models two fluid plasma using asymptotic expansions for bounded plasma driven by an rf current. The dynamics of plasma is determined separately in the bulk, transition and sheath regions. In the computational approach, Nitschke and Graves (1994) have compared the PIC and fluid models for rf discharge of helium gas for a range of pressure (50mTorr-250mTorr) and electrode gap (40mm to 120mm). Xiang and Waelbroeck (2003) investigated the ion dynamics in presheath and sheath region using numerical and analytical methods for collisionless plasma. Zhang et.al. (2004) also have simulated a collisionless sheath

behavior based on Boltzman approximation for electrons. Hammond, et. al. (2002) have obtained solution for low pressure helium discharge. Bose, et. al. (2000) analyze non-collisional sheath characteristics by applying boundary conditions at a pre-determined sheath-presheath edge.

But for a few exceptions (Roy et. al., 2003 and Kumar and Roy, 2005), the number of attempts to model discharge in one-dimension for argon in particular is comparatively less. There have been some published reports on simulation of discharge in more realistic two-dimensional geometries. Boeuf (1988) developed a self-consistent model for dc glow discharges in cylindrical geometry less than two decades ago. Passchier and Goedheer (1993) present a fluid model for argon in a reactor geometry using drift-diffusion approximation and an effective electric field assumption. Boeuf and Pitchford (1995) also present an elaborate fluid model for argon rf plasma in a GEC reference cell. Kim and Economou (2003) investigated plasma formation over an inhomogeneous flat wall. More recently, Surzhikov and Shang (2004) have studied discharge modification in the presence of applied magnetic field for nitrogen in a symmetric two-dimensional chamber.

Thesis Summary

Despite these attempts, self-consistent approaches for simulation of rf induced plasma interactions with fluids remain in an early stage of development. The present effort aims to develop a numerical framework for modeling and understanding ionized gas dynamics in multi-dimensions. The approach is general and can be used to study discharge for varying pressure, gases and other discharge conditions. The model also forms the foundation of a versatile first-principles based methodology. First, the plasma

and sheath characteristics of a one-dimensional discharge configuration in argon are studied under dc and rf input conditions. The two-dimensional two-fluid plasma formation over a coated flat plate is then investigated for three different cases. The numerical algorithm is formulated using finite element method and first benchmarked for plasma formed between symmetric electrodes in nitrogen gas. Discharge characteristics of plasma for electrode-insulator configuration are then analyzed under steady and transient conditions using argon as a working gas. The effect of magnetic field on electric potential and charge difference is studied for a thin electrode.

Chapters in Thesis

Summary of the remaining thesis chapters is as follows:

- Chapter II describes in detail the governing equations, the development of the finite element algorithm, FE basis functions.
- Modeling of two-fluid fully ionized plasma in a direct current discharge in one dimension is presented in Chapter III. It includes the geometry details and boundary conditions.
- Chapter IV covers formulation of two cases of radio frequency driven discharge for a one-dimensional bounded plasma in the collisionless and collisional regime.
- Chapter V presents the two-dimensional discharge characteristics of plasma formed in inhomogeneous geometries under steady and unsteady input voltages.
- Finally conclusions and recommendations for future work are given in Section VI.

II. HYDRODYNAMIC MODELING

A hydrodynamic model has been developed to simulate multifluid plasma in low-pressure regime. The model uses an efficient finite element algorithm. The following sections detail the governing equations, boundary conditions and the algorithm implementation procedure. Nomenclature for all the variables, functions and constants are given in Appendix A.

Governing Equations

The time-dependent, Navier-Stokes (NS) equation set in the form of mass and momentum conservation law for ionized gases are given in Equations 2-4. It represents a basic framework and is suitably altered for different cases under consideration in the subsequent chapters.

Conservation of number density *N*:

$$\frac{\partial n}{\partial t} + \nabla.(nV) = S \tag{2}$$

Conservation of momentum:

$$M\left(\frac{\partial V}{\partial t} + V.\nabla V\right) = -\frac{1}{n}\nabla.P + qE - M\nu V \tag{3}$$

Here ν is the momentum transfer frequency and P is the species pressure defined by equation of state ($P=NkT$). Under the drift-diffusion approximation, this equation may be simplified by ignoring the inertial and temporal derivative terms as:

$$\nu V = -\frac{1}{n}\nabla.P + qE \tag{4}$$

These equations are combined with an equation for electrostatic field in the form of Poisson equation to solve for species density, velocity and electric potential for different applications. The Poisson equation is a second order partial differential equation similar to the Laplacian equation with non-zero coefficient, $\nabla^2\phi = -\rho/\varepsilon$, where ϕ is the potential, ρ is the net charge and ε is permittivity.

The system of Equations 2-4 is normalized using the following expressions: $\tau = 2\pi ft$, $z=x/d$, $N_e=n_e/n_0$, $N_i=n_i/n_0$, $u_i=V_i/V_B$ and $u_e=V_e/V_B$ and $\phi=e\varphi/T_e$, f is the applied frequency, d is a reference length which is usually a domain length in the geometry, n_0 is a reference density and the Bohm velocity $V_B = \sqrt{T_e/m_i}$.

Note on Ionization and Recombination

The source and sink term appearing in the continuity Equation 2 of species density is in the form of ionization and recombination.

$$S = \alpha n_e - \beta n_e n_i \tag{5}$$

where α is ionization rate in /s and β is the recombination coefficient in m^3/s. Different ways of estimating the ionization rate have been used in discharge modeling. In some of the models, like those by Nitschke and Graves (1994), the rate takes a simple Arrhenius form in terms of ionization threshold and electron temperature. Expressing ionization rate as a function of reduced effective field (obtained based on a solution from electron energy equation) is yet another approach. So far, there have not been systematic comparisons between these methods and its impact on discharge computations. Here, the rate constants for ionization are functions of electron energy. These coefficients have

been measured under steady state condition from a dc discharge in Argon Townsend and time of flight experiments as a function of *E/p*. The ionization rate is calculated by multiplying drift velocity and Townsend ionization coefficient. The following diagrams in Figure 1 quantitatively show variation of recombination and ionization coefficients in an argon discharge from literature.

The three body electron-ion recombination rate coefficient for argon has been calculated within the range of electron number densities $l0^{10}$ -10^{16} cm^{-3} and electron temperatures of 2000 K–16,000 K by Wanless (1971) as plotted in Figure 1(i). It can be observed that for temperature of 1eV and beyond, the recombination coefficient is of the order of 10^{-13}. On the other hand, the ionization rate increases with electron temperature as given by Figure 1(b) (Boeuf and Pitchford, 1995). The rate of production is higher for 6 eV or more. The time-averaged ionization rate between two electrodes calculated based on Townsend ionization for low-pressure argon is given by (Paranjpe et. al., 1990) and has been plotted in Figure 1(b).

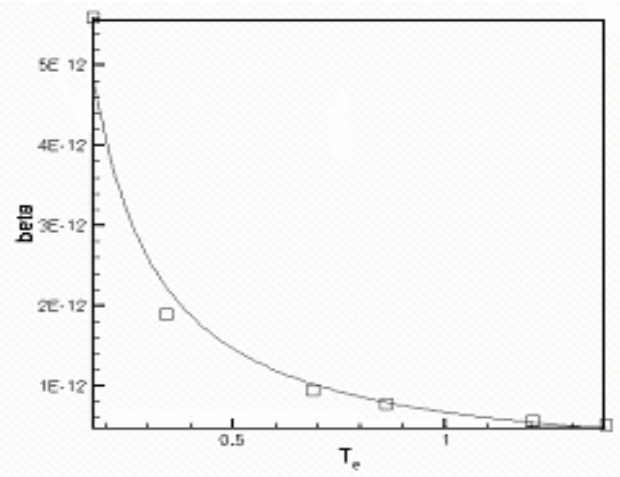

(a)

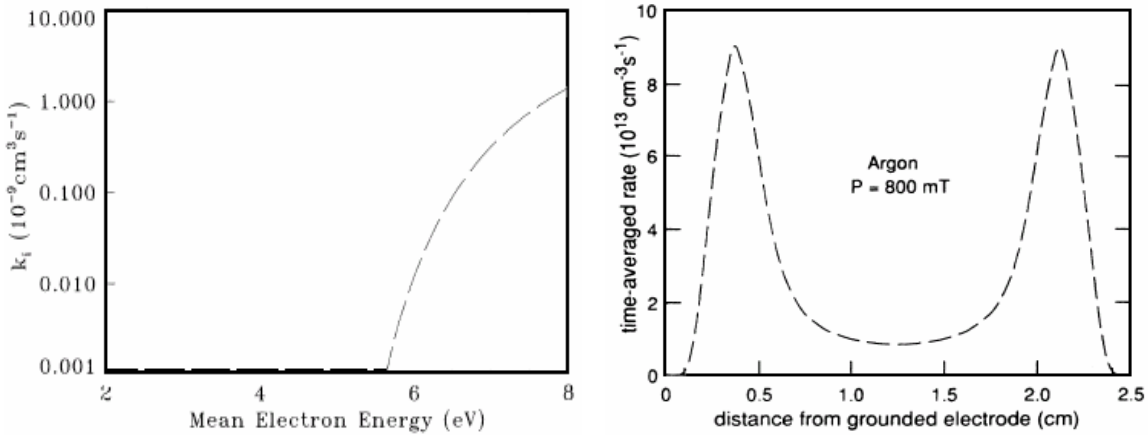

(b)

Figure 1. (a) Recombination coefficient (Wanless, 1971) and (b) variation of ionization rate with electron temperature (Boeuf and Pitchford, 1995) and with space (Paranjpe et. al., 1990).

Finite Element Algorithm

The finite element method (FEM) is used here for solving partial differential equations (PDE) approximately. FEM has been used since 1950 for analyzing structural systems. Beginning in the early 70's it has also been utilized for analyzing fluid thermal systems. In FEM, solutions are approximated by rendering the partial differential

equation (PDE) into an equivalent ordinary differential equation (ODE), which is then, solved using standard techniques. In the finite-element method, a distributed physical system to be analyzed is divided into a number of discrete elements. With the development of weighted-residual criteria it has also found significant usage in fluid mechanics and heat transfer applications. Weighted Residual Method (WRM) assumes that the solution to the parent PDE/ODE can be approximated with a continuous or piecewise continuous analytic function. Depending on the WRM maximization, numerical techniques like finite volume, finite element and spectral volume methods may be used. The numerical development of this thesis is anchored in an existing finite element based multi-scale ionized gas (MIG) flow solution platform that has been utilized for a range of applications including electric propulsion, design optimization and micro/nano-scale flow analysis (Roy and Pandey, 2002, Balagangadhar and Roy, 2001, & Cooper et. al., 2004).

The Equation System 2-4 can be written as a general and more concise convection-diffusion type equation:

$$L(\boldsymbol{q}) = \frac{\partial \boldsymbol{q}}{\partial t} + \frac{\partial (\boldsymbol{f} - \boldsymbol{f}_j^v)}{\partial x_j} - s = 0 \tag{6}$$

where $\boldsymbol{q}$ is the state variable, $\boldsymbol{f}$ is the kinetic flux vector, $\boldsymbol{f}^v$ the dissipative flux vector and s is the source term.

Galerkin Weak Statement

The fundamental principle underlying the finite element method is the construction of a solution approximation as a series of assumed spatial (test) function multiplied by a set of unknown expansion coefficients such as the Galerkin Weak Statement, acronym GWS (Baker and Pepper, 1991), which is followed in this numerical

work. Other categories of approximation functions, which are applied in WRMs, are sub-domain method, collocation and least square method.

Any real world smooth problem distributed over a domain x_j can be approximated as a Taylor or power series of known coefficients a_i and functions $\phi_i(x_j)$:

$$L(q) = \sum_i a_i \phi_i(x_j) \tag{7}$$

where a_i are unknown coefficients and $\phi_i(x_j)$ are known functions of x_j. The GWS approach requires that the measure of the approximation error should vanish in an overall integrated sense. This gives a mathematical expression for minimization of the weighted residual over the domain for Equation 6 as,

$$WS = \int_{\Omega} wL(q)d\Omega \equiv 0 \tag{8}$$

Here, Ω defines the domain for the problem statement and w is the weight function set. For the Galerkin condition to hold true, the weight function is made identical to the corresponding trial function set ϕ for the approximation of state variables. Equation 8 guarantees that the associated approximation error is a minimum since it is orthogonal to the trial function set ϕ. The term "weak statement" signifies that the differentiability requirement for the approximation function is weakened by one order.

Finite Element Basis Functions

The finite element basis is a set of polynomials generally distributed uniformly on every subdivision (*finite element*) of the solution domain, Ω created by placing nodes for better resolution and hence constructing the domain discretization Ω_h (Baker and Pepper, 1991). Discretization for the domain is a fundamental concept of finite element analysis since it simplifies the construction of a wide range of suitable trial functions, ϕ. The set of

functions associated with the trial function, ϕ, that spans over a single generic element Ω_{el} are defined as the *finite element basis*. The finite element basis, N_k maybe Chebyshev, Lagrange or Hermite interpolation polynomials complete to degree k based on the problem statement (one, two or three- dimensional).

The discrete approximation of the spatially discretized domain Ω^h yields a union of elements Ω_{el} as shown:

$$\Omega^h = \bigcup_{el} \Omega_{el} \tag{9}$$

Similarly the integrated variables can be represented as the union of spatially and temporally discretized elements:

$$q(t, x_j) \approx q^h(t, x_j) = \bigcup_{el} q_{el}(t, x_j) = \bigcup_{el} N_k(x_j) Q_{el}(t, x_j) \tag{10}$$

The spatially discretized finite element basis definition yields:

$$Q_{el} = \{N_k\}\{Q\}_{el} \tag{11}$$

The finite element basis functions, N_k for k=1,2 and their corresponding shapes based on Lagrange interpolation polynomials in local and global coordinates for one and two dimensions are given in Figures 2-5. Note that higher degree k of the basis will generally involve higher number of supporting nodes in the element.

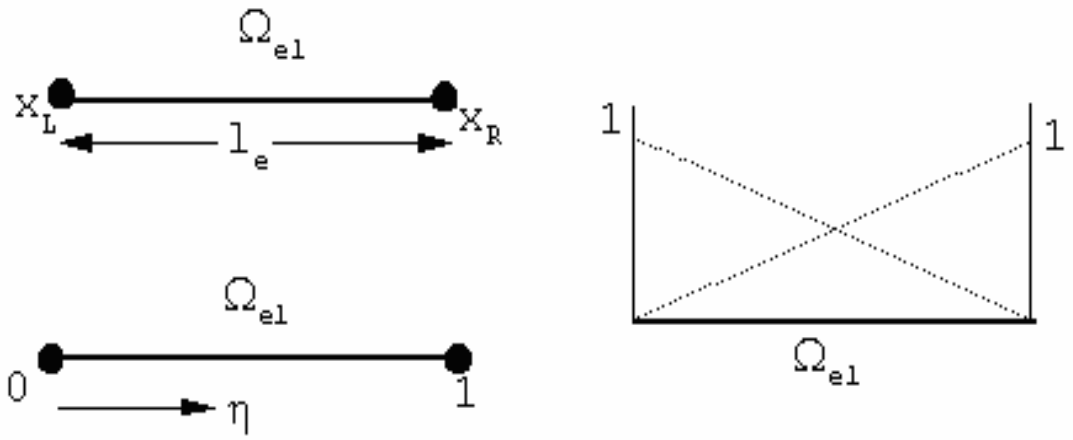

$$\textit{Basis Function}: \ \{N(\eta)\} = \begin{Bmatrix} 1-\eta \\ \eta \end{Bmatrix}$$

Figure 2. One dimensional linear element Ω*el* for linear basis.

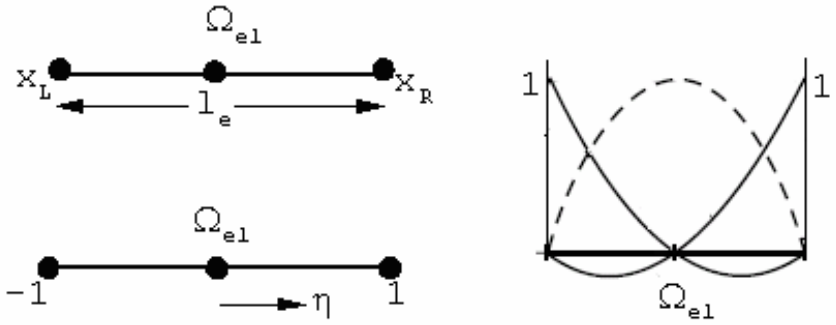

$$\textit{Basis Function}: \ \{N(\eta_1,\eta_1)\} = \begin{Bmatrix} \eta_1(2\eta_1-1) \\ 4\eta_1\eta_2 \\ \eta_2(2\eta_2-1) \end{Bmatrix}$$

Figure 3. One dimensional quadratic element Ω*el* for quadratic basis.

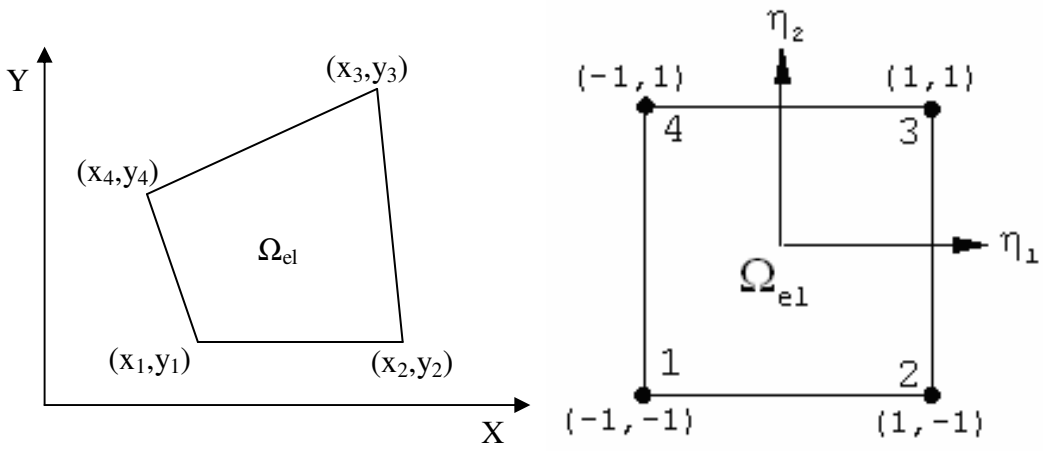

$$\textit{Basis Function}: \ \{N(\eta)\} = \frac{1}{4}\begin{Bmatrix} (1-\eta_1)(1-\eta_2) \\ (1+\eta_1)(1-\eta_2) \\ (1+\eta_1)(1+\eta_2) \\ (1-\eta_1)(1+\eta_2) \end{Bmatrix}$$

Figure 4. Bilinear basis quadrilateral element $\Omega_{el.}$

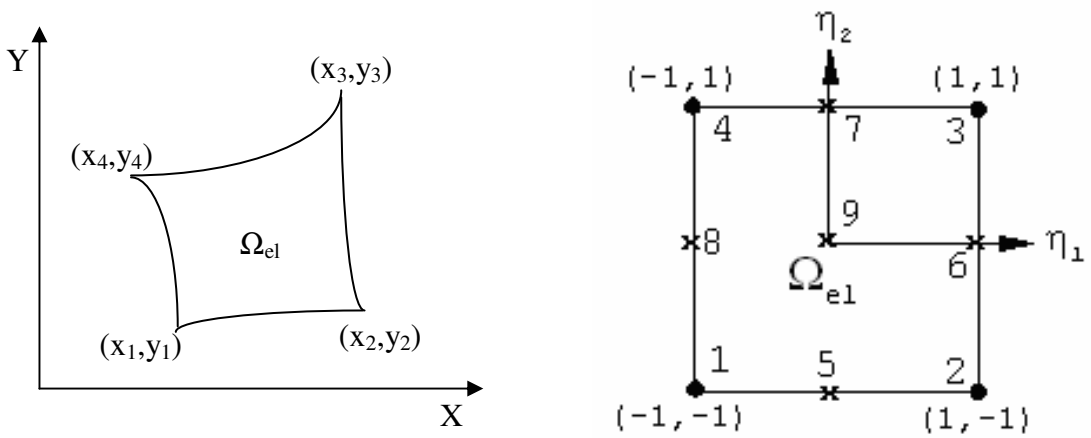

$$Basis\ Function:\ \{N(\eta_1,\eta_2)\} = \frac{1}{4}\begin{Bmatrix} (1-\eta_1)(1-\eta_2)(\eta_1\eta_2) \\ (1+\eta_1)(1-\eta_2)(-\eta_1\eta_2) \\ (1+\eta_1)(1+\eta_2)(\eta_1\eta_2) \\ (1-\eta_1)(1-\eta_2)(-\eta_1\eta_2) \\ 2(1-\eta_1^{\,2})(1-\eta_2)(-\eta_2) \\ 2(1-\eta_1)(1-\eta_2^{\,2})(\eta_1) \\ 2(1-\eta_1)(1-\eta_2)(\eta_2) \\ 2(1-\eta_1)(1-\eta_2^{\,2})(-\eta_2) \\ 4(1-\eta_1^{\,2})(1-\eta_2^{\,2}) \end{Bmatrix}$$

Figure 5. Full biquadratic quadrilateral element $\Omega_{el.}$

Solution Methodology

Independent of the physical dimension of Ω, and for general forms of the flux vectors, the semi-discretized weak statement of Equation 6 always yields an ordinary differential equation (ODE) system of the following form:

$$WS^h = M\frac{dU}{dt} + R(Q) = \{0\} \tag{12}$$

Here, Q is the time-dependent finite element nodal vector, $M = S_{el}(M_{el})$ is the "mass"

matrix associated with element level interpolation, while *R* carries the element convection information and the diffusion matrix resulting from genuine (non-Eulerean) or elemental viscosity (natural or artificial) effects, and all known data. The time derivative *dU/dt,* is generally replaced by using a θ-implicit time integration procedure and the terminal ODE is usually solved using the following Newton-Raphson (NR) scheme:

$$\begin{aligned} Q_{t+1}^{i+1} &= Q_{t+1}^{i} + \Delta Q^{i} = Q_t + \sum_{p=0}^{i} Q^{p+1} \\ \left[M + \theta \Delta t (\partial R / \partial Q)\right] \Delta Q^{i} &= -R(Q) \end{aligned} \tag{13}$$

where *i* is the iteration, and t is the timestep. The choice of time step is dictated by the Courant-Fredrich-Levy condition (Richtmyer and Morton, 1967).

The solution is declared convergent when the maximum residual for each of the state variables becomes smaller than a chosen convergence criterion. Here, the convergence of a solution vector U on node *j* is defined as the norm:

$$\frac{\left\| Q_j - Q_{j-1} \right\|}{\left\| Q_j \right\|} \leq \varepsilon \tag{14}$$

Here, an implicit (θ=1) time stepping procedure is employed. There are obvious numerical issues associated with calculation of the "jacobian", ∂R/∂Q within sufficient accuracy.

For steady state problems, a procedure analogous to relaxation methods utilized for finite difference scheme, is employed. Equation 6 can be modified in the following form:

$$\frac{\partial f}{\partial x_j} - s - \varepsilon \frac{\partial^2 q}{\partial x_j^2} = 0 \tag{15}$$

where ε is a diffusion perturbation parameter that can be varied separately for each state variable. As $\varepsilon \to 0$, Equation 15 reverts back to steady state form of Equation 6. Initially ε is set to a sufficiently high value so as to generate a diffused but stable convergence to steady state solution. Progressive reduction of ε is carried out until the final steady state solution with $\varepsilon \to 0$ is achieved.

The ionized gas is numerically modeled using the finite-element based Multiscale Ionized Gas (MIG) flow code. The code is modular and separate subroutines can be written to model different physics. The sequence of procedure to update solution variable $\boldsymbol{q}$ in a given iteration is presented in the form of a flowchart in Figure 6. For the one-dimensional formulation, the code generates element matrix for each of the elements into which the domain is discretized and adds elemental information appropriately into a global stiffness matrix by mapping indices between local to global matrix. The Newton-Rhapson scheme for non-linear system is used and resulting matrix may be solved using non-iterative decomposition (LU) or iterative pre-conditioning (GMRES or BiCGSTAB) schemes.

Figure 6 depicts the flow of sequence for a single iteration of the solution process as implemented in the code. The element stiffness matrix is created within a sub-loop and is successively assembled into a global stiffness matrix which is solved using a Newton-Rhapson nonlinear scheme to increment the solution variable. One main disadvantage of formation of this full global matrix is the limitation in memory allocation depending on the computational capacity of the system used. Consider a problem with a mesh consisting 41×41 nodes and 3 dependent variables. The non-linear N-R for this problem requires a matrix with 5043 columns, to be formed for every iteration and whose number

of rows depends on the bandwidth of the problem, Figure 6(a). This number becomes unmanageable as problem degrees-of-freedom (size) increases. The maximum allowed bandwidth is machine dependent which limits the computational capability. Also, due to the nature of finite element algorithm and elemental and nodal numbering scheme followed, the resulting matrix becomes sparse in nature for higher dimensional formulations. As a viable remedy, an iterative sparse matrix solver called Generalized Minimal RESidual (GMRES) has been implemented. The assembly procedure involves storing only the non-zero elements of the matrix ($\partial R/\partial q$) in the form of a linear array and the corresponding row and column locations using an incremental flag as represented by the block as shown in Figure 6(b). The program progresses through each element; the information is added appropriately to the particular location in this array thus eliminating the formation of a large global matrix.

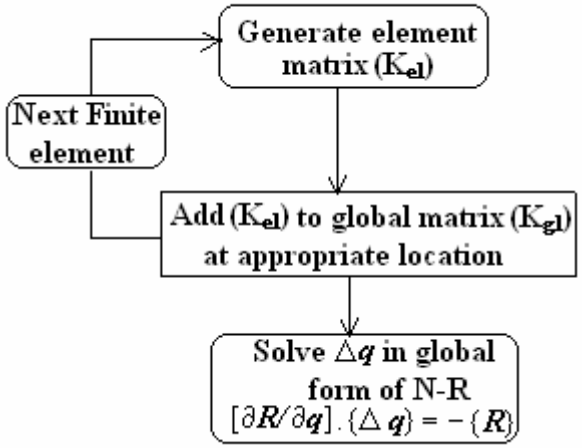

(a)

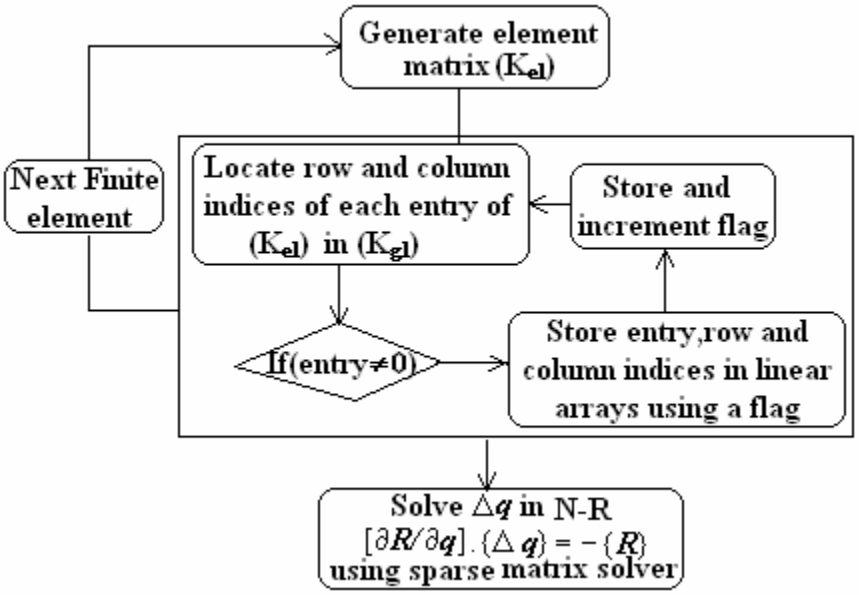

(b)

Figure 6. Flow charts for (a) global matrix assembly formation and (b) alternative element assembly procedure used for GMRES.

A comparison between the two sequences, shown in Figure 6, is done for varying mesh size keeping all other parameters and looping schemes as same. Figure 7 plots the computational time for assembly and solver separately. It is found that the algorithm which does not involve global matrix formation works better for larger number of nodes.

The comparison of the solver time is also shown in Figure 7(b) for varying mesh measure. The scheme involving formation of global matrix and decomposition solver is comparable only for mesh with 501 or fewer nodes.

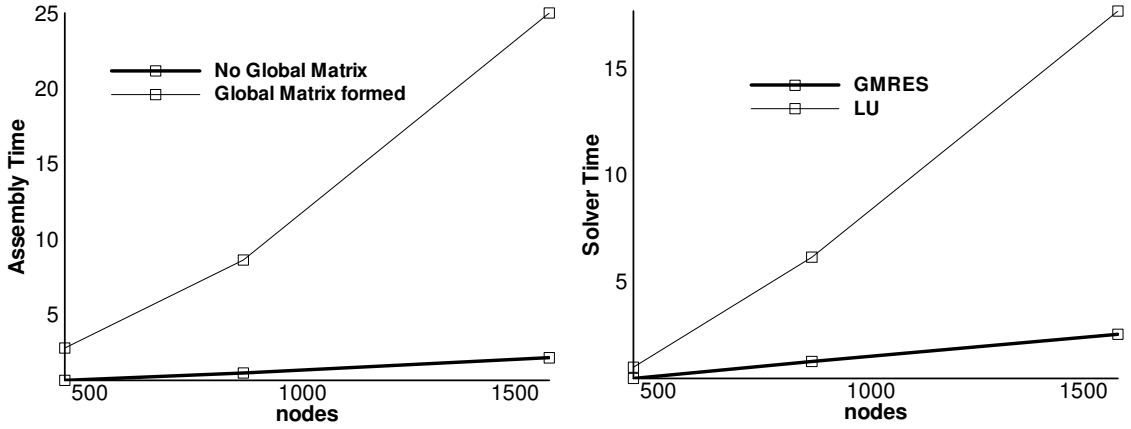

Figure 7. Comparison of assembly and solver time for the assembly methods in Figure 6.

Algorithm Stability

The stability of an algorithm can be investigated from its amplification factor G^h and the relative phase velocity Φ^h. Though the dynamics of the charge species have not yet been introduced elaborately until this point, for exploratory purposes, the drift-diffusion approximation for electrons and ions is used. Based on the finite element stencil and using Fourier representation (=$e^{iw(j\Delta x-Un\Delta t)}$), one may derive the following amplification factor for ions:

$$\frac{\partial}{\partial x}(n_i\mu_i E - D_i\frac{\partial n_i}{\partial x}) = n_e S$$

$$G^h = \left[1 - 3iCf(m\Delta z) - S\Delta t(\cos\theta + i\sin\theta)\right]^{-1} \tag{16}$$

with the magnitude $\left|G^h\right| = \left((1 - S\Delta t\cos\theta)^2 + (3Cf(m\Delta z) + S\Delta t\sin\theta)^2\right)^{-0.5}$

and the phase velocity $\Phi^h = \tan^{-1}\left[\frac{(3Cf(m\Delta z) + S\Delta t \sin\theta)}{(1 - S\Delta t \cos\theta)}\right] \Big/ -Cm\Delta z$, (17)

while those for electrons are:

$$\frac{\partial}{\partial x}(-n_e \mu_e E - D_e \frac{\partial n_e}{\partial x}) = n_e S$$

$$\begin{aligned} G^h &= \left[1 - 3iCf(m\Delta z) - S\Delta t\right]^{-1} \\ \left|G^h\right| &= \left[(1 - S\Delta t)^2 + (3Cf(m\Delta z))^2\right]^{-0.5} \end{aligned} \quad (18)$$

and $\Phi^h = \tan^{-1}\left[\frac{3Cf(m\Delta z)}{(1 - S\Delta t)}\right] \Big/ -Cm\Delta z$ (19)

In Equations 16-19, m is the wave number, Δz is the length of an element, *C* is the Courant number, $f(m\Delta z) = \sin m\Delta z \big/ \left(2 + \cos m\Delta z\right)$ and $\theta = -(u_e^h - u_i^h)m(n+1)\Delta t$ is the relative velocity phase angle. Here, the case of θ = 0 has been analyzed, which includes both ions and electrons. The algorithm is stable if the algorithm amplification factor $|G^h| \leq 1$ (Roy, 1994). One prefers $\Phi^h \sim 1$ to minimize the loss of information during solution process. Figure 8 plots $|G^h|$ as a function of $m\Delta z$ for two values of S and C. Obviously for a higher value, $S_2 = 500$, the solution becomes unstable. The numerical difficulty may be handled by appropriate selection of Courant number and introduction of artificial diffusion. The result however gives an insight to the increasing instability of the standard solution procedure about the bulk-sheath transition region.

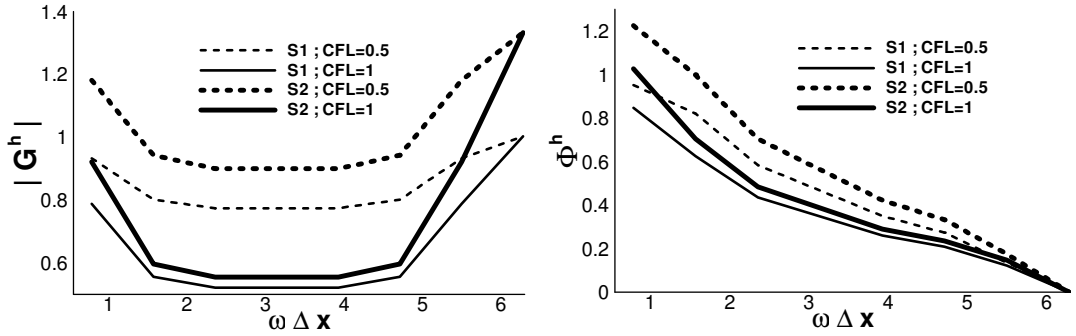

Figure 8: Algorithm amplification factor ($|G^h|$)and relative phase velocity (Φ^h) for varying Courant numbers (C=0.5 and 1) and ionization rates S1 = 5 and S2 = 500.

Note on Scales

Due to a vast difference in mass between electrons and ions, the response of each of the species to any external force is drastically different. The electron and ion plasma frequencies are given:

$$\omega_{pe} = \sqrt{\frac{N_e e^2}{\varepsilon m_e}} \text{ and } \omega_{pi} = \sqrt{\frac{N_i e^2}{\varepsilon m_i}} \tag{20}$$

Clearly, the frequency of electrons is much higher in a quasi-neutral $(N_i \approx N_e)$ plasma. Hence, they almost respond immediately in the time frame of the more massive ions. As a consequence, two different timescales arise in the problem with several orders of magnitude difference between them. The present algorithm involves a self-consistent solution procedure where both electron and ion dynamics are captured simultaneously. Due to inherent coupling of variables in the plasma, the non-linearity may affect convergence of the solution. Another method may be to employ a conventional multi-scaling scheme. In such a scheme, the ion dynamics are solved once in every tens or hundred timesteps of solution for electrons.

The presence of varying timescales within the model, as can be understood from this section poses a significant numerical complexity. Another challenging aspect is the resolution of spatial scales. The sheath which is a region of large property gradients extends only few Debye lengths into the plasma as compared to the physical domain of the plasma. Hence resolving the spatial nature of this sub-millimeter scale sheath needs separate attention.

III. MODELING OF ONE DIMENSIONAL DISCHARGES

Direct Current Glow Discharge

A direct current (dc) discharge forms plasma, sustained by a direct current through an ionized medium. A high potential difference applied between electrodes immersed in a gaseous environment results in the electrical breakdown of the gas.

These discharges are characterized by continuous steady currents and are mostly sustained by secondary emissions. The theoretical prediction of dc discharges based on experimental data was reported as early as 1962 (Ward, 1962).

Problem specification

To understand the dynamics of the sheath, we hydro-dynamically model two-fluid bounded plasma under direct ionization when ionization rate is considered constant. Only a symmetric half of the plasma is considered and all the boundary conditions are imposed based on quasi-neutral properties at the plasma center.

For steady state conditions, the governing system of equations is obtained from Equations 2-4 for cold ion case.

Continuity equation:

$$\frac{d}{dx}\left(N_i V_i\right) = N_e \tag{21}$$

Momentum equation:

$$V_i \frac{dV_i}{dx} - E + \frac{V_i}{N_i} N_e = 0 \tag{22}$$

Poisson equation:

$$\frac{dE}{dx} - \varepsilon^{-2}(N_i - N_e) = 0 \tag{23}$$

where $\varepsilon = 4.036 \times 10^{-3}$. The system of equations is completed using a Boltzmanian approximation for electrons:

$$N_e = e^{-\phi} \tag{24}$$

The geometry consists of domain that extends up to ~0.7. x=0 is the center of the plasma where the following boundary conditions are employed.

$N_i(0)=1.0$, $V_i(0)=0.0$, $E(0)=0$, $\phi(0)=0$

This system of equation cannot be solved analytically due to the singularity in center of plasma where ion velocity is assumed zero (Sternberg and Godyak, 1996). The System 21-24 is solved using finite element algorithm explained in Part I.

The weak statement formulation for the equation system is as follows

Continuity equation:

$$S_e\left(\int_\Omega V_i\psi\frac{d\psi^T}{dx}dx\{N_i\}_e + \int_\Omega N_i\psi\frac{d\psi^T}{dx}dx\{V_i\}_e - \int_\Omega \psi e^{-\phi}dx\right)_e = F_N \tag{25}$$

Momentum Equation:

$$S_e\left(\int_\Omega V_i\psi\frac{d\psi^T}{dx}dx\{V_i\}_e - \int_\Omega \psi\frac{d\psi^T}{dx}dx\{\phi_i\}_e + \int_\Omega \frac{e^{-\phi}}{N_i}\psi\psi_T dx\{V_i\}_e\right)_e = F_V \tag{26}$$

Poisson equation:

$$S_e\left(\int_\Omega \psi\frac{d\psi^T}{dx}dx\{E_i\}_e - \varepsilon^{-2}\int_\Omega \psi\psi^T dx\{N_i\}_e + \varepsilon^{-2}\int_\Omega \psi\psi^T dx\{N_e\}_e\right)_e = F_E \tag{27}$$

and equation showing the derivative relation between ϕ and E is

$$S_e\left(-\int_\Omega \psi \frac{d\psi^T}{dx} dx\{\phi_i\}_e + \int_\Omega \psi\psi^T dx\{E_i\}_e\right)_e = F_\phi \tag{28}$$

The mesh consists of 900 linear elements. The elements are refined towards the wall to capture the larger gradient changes thus approximating the curve in a better way.

Results and discussion

The first order system of Equations 25-28 is solved using linear interpolation polynomials. As described in the previous chapter an artificial diffusion parameter (ε) is introduced to get a diffused initial condition. Final steady state solution is achieved when $\varepsilon \to 0$.

In the process of obtaining the numerical solution, due to the singularity near the center of plasma, unrealistic local numerical oscillation near x=0 may be observed. This is more prominent in the ion number density profile within range of 0.01 spatially. A simple algebraic calculation was performed on the mesh. The Equation System 21-24 at second node (at distance of the mesh measure, h) reduces to:

$$N_i V_i = he^{-\phi} \tag{29}$$

$$V_i^2 + h(V_i / N_i)e^{-\phi} = \phi \tag{30}$$

$$\phi = ah^2(N_i - e^{-\phi}) \tag{31}$$

If $V_i > h$, from Equations 29-31, N_i can be evaluated as sum of $e^{-\phi}$ and a function of h, which may give a value greater than one. This dependence on mesh measure can also be related to the refinement of mesh near the wall increasing the nodal distance near center. Proper choice of initial condition is also necessary.

The progress of solution is represented in terms of the residual and solution norm as plotted in Figure 9(a) and (b) respectively. The solution converges to steady state in about 80 iterations. The simulation (assembly and solver) takes just few minutes in actual time. Though artificial schemes were employed to get a better initial condition before the actual simulation was performed, the method proves as a simple, fast and cost-effective tool to predict the discharge characteristics.

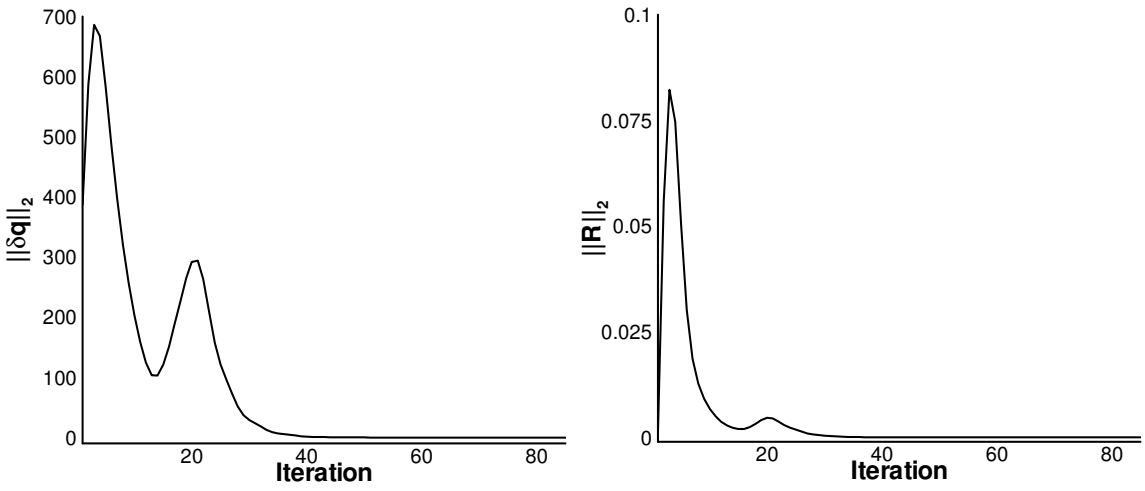

(a) (b)

Figure 9. L_2 norm of (a) solution increment and (b) solution residual.

The results of the solution are presented in Figure 10(a) to 10(c).

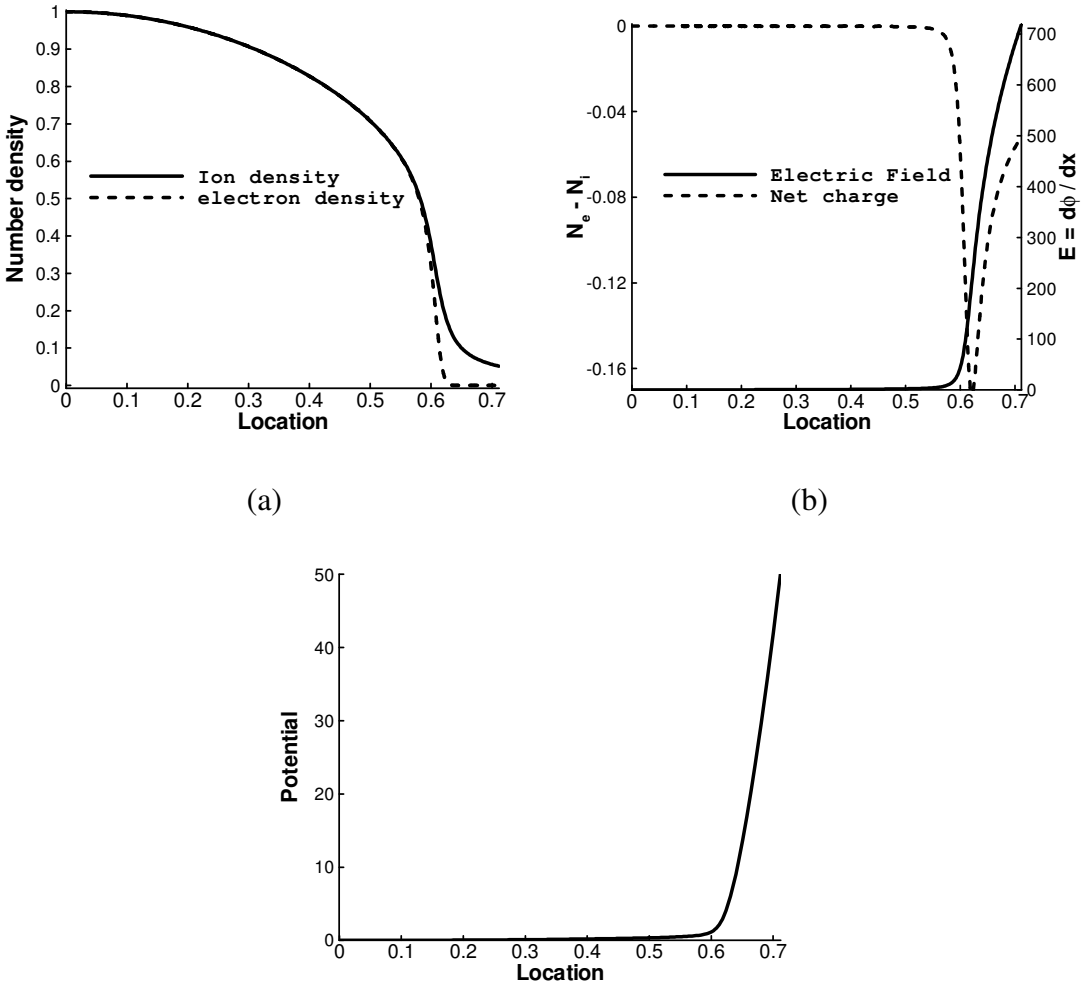

Figure 10. Plasma solution using finite element methods (a) normalized species density (b) normalized electric field and net space charge (c) normalized electric potential.

Two distinct regions may be observed from Figure 10(a), the quasi-neutral plasma where $N_i \approx N_e$ and the layer of sheath attached to the wall where $N_i >> N_e$. Based on the Bohm velocity of ions, the sheath edge is identified at 0.58. Here, a case of direct ionization is assumed where the ionization rate is assumed constant and is of the order

~10^4. We see the tail of electron density close to the wall reaching values close to zero. The Boltzmanian distribution assumed for electrons explains this behavior. Note that this assumption is true for isothermal, collision less and unmagnetized plasma. The electric field arising out of this charge separation is plotted in Figure 10 (b). The field rises to a normalized value close to 700 in the sheath. As can be seen, there is two orders of difference in magnitude between field in the sheath and that in the bulk. Hence from the ion momentum equation, it can be concluded immediately, that the motion of ions inside the sheath is mostly electro-dynamic. The net charge distribution or the space charge separation is plotted in Figure 10(b). As one approaches the sheath edge, there is an abrupt drop in the charge difference within a small spatial extent. This is the region of pre-sheath where separation in ion and electron density curves begins and where electron density is just less than ion density. The applied potential reaches a value of 50 (normalized) at the wall.

Radio Frequency Discharges

The load factor (ratio of electric field to Lorentz force) for dc sheath application is of the order 1, far from the Stoletow point, thus unsuitable for ionization purposes. A popular alternative method is through the application of unsteady rf fields with frequencies in range of 1 to 100 MHz. Understanding rf induced sheath dynamics near the surface of an electrode has a strong effect on both volume ionization efficiency and on energy interactions with the neutral gas flow. Specifically, with the recent progress in rf plasma-based boundary layer flow control (Enloe et. al., 2004), where the fundamental mechanisms remain unclear, the understanding of rf plasma and its bounding sheath has become crucial. This requires a theoretical modeling technique that is geometry versatile

and time accurate. Here, we attempt to model bounded plasma up to and including the sheath near the electrodes at 0.1 torr pressure.

At low discharge pressures (~millitorr) applicable to the semiconductor and material processing industries, the dynamics of rf sheath has been studied by early researchers, Zhang et. al. (2004), Roy et. al. (2003) and Hammond et. al. (2002), to name a few. There are a few methods for modeling plasma-wall under applied potential. These include the bulk plasma model, the step-front-electron sheath model and the asymptotic expansion method. These theoretical advances notwithstanding, a self-consistent simulation for rf driven plasma-wall interactions remains a quest. In a self-consistent plasma-wall model followed in some earlier works (Roy et. al., 2003 & Hammond et. al., 2002), the space charge effect is incorporated for the entire discharge. The sheath structure is investigated in the post-processing phase unlike the patching/matching techniques where bulk plasma forms a boundary condition to sheath solution.

Recently, two such plasma-wall models have been reported for two-component fully ionized plasma (Roy et. al., 2003) and three component partially ionized gas (Roy and Gaitonde, 2004). The two-fluid model was applied to predict the rf discharge inside a tube filled with argon gas. The three-fluid model characterized the effect of volume ionization on the neutral helium gas flow between two dielectric coated electrodes at atmospheric pressure. The intention is to complement experimental efforts by providing a suitable tool to explore flow control concepts in future design and development.

Following an earlier work, (Roy et. al., 2003) a detailed study of the space charge effect in a two-fluid capacitive rf plasma-wall system in the presence and absence of collisional impact ionization is presented here.

Problem specification

Figure 11 shows the circuit for a typical capacitive rf discharge. A time varying potential is applied at the right electrode through a blocking capacitor C. The left electrode is grounded. Two-fluid plasma consisting of electrons and ions is considered. The unsteady continuity and momentum (drift-diffusion) equations are solved simultaneously with the Poisson equation. The transverse extent of the discharge is assumed to be much larger than the inter-electrode distance and hence a one-dimensional model is considered sufficient. When the ion mfp is comparable or less than maximum sheath width, ions involve in more than one ionizing collisions. It has been found that for pressure less than 0.003 torr for argon, collisionless approximation is valid. For conditions above 3mtorr upto 0.15 torr, argon falls in the lower end of collisional regime. Hence, the argon plasma at 0.1 torr is collisional. However, to identify the effects of collision in the space-charge separated sheath region, the problem is first considered without the collision and then with the collisional effects. Hereafter, Case A will be referred for the collisionless model, while Case B represents the collisional problem.

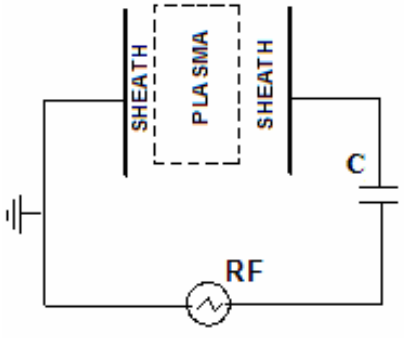

Figure 11. Schematic of the capacitive rf discharge.

The following fluid equations are used. The continuity equation for electron (e) and ion (i) number densities is given:

$$\frac{\partial n_i}{\partial t} + \frac{\partial \Gamma_i}{\partial x} = n_e S$$
$$\frac{\partial n_e}{\partial t} + \frac{\partial \Gamma_e}{\partial x} = n_e S \quad \text{where flux, } \Gamma = nV \tag{32}$$

Here, n is the species density and V is the species hydrodynamic velocity. A collisionless condition (zero ionization) is ensured in case A. For case B, the ionization frequency is governed by the Townsend equation:

$$S = Ae^{-B/(E/p)^{0.4}} p\Re \tag{33}$$

where A and B are known for the gas[15]. $\Re = \mu_e E$ (which has a dimension of velocity, cm/s) may be viewed as the speed of ionization that models the spatially and temporally varying ionization.

The electrons flux is governed by:

$$\Gamma_e = -n_e \mu_e E - D_e \frac{\partial n_e}{\partial x} \quad \text{with } D_e = \mu_e T_e/e \tag{34}$$

The electron mobility μ_e is given by (Ward, 1962) $p\mu_e = 3\times10^5 cm^2 V^{-1} s^{-1} Torr$, at p=0.1 Torr. The electron temperature (T_e) is 1 eV. For ions, in case A, the inertial term is included in the formulation of its momentum:

$$\frac{\partial V_i}{\partial t} + V_i \frac{\partial V_i}{\partial x} = \frac{e}{m} E - \gamma_i V_i \tag{35}$$

While for case B, the flux can be derived from the drift velocity and hence:

$$\Gamma_i = n_i \mu_i E - D_i \frac{\partial n_i}{\partial x} \tag{36}$$

Here electric field $E=-\partial\varphi/\partial x$. For cold ions at $T_i = 0.025$ eV, $D_i = 200\,\mathrm{cm}^2/\mathrm{s}$. The ion mobility μ_i is based on the degree of ionization, electric field and pressure (Ward, 1962). While one may include the inertia terms to get a slightly improved solution, at 0.1 torr pressure argon plasma sheath is collisional (Liebermann and Lichtenberg, 1994) and the drift-diffusion approximation is reasonable and computationally efficient. Under the effect of collisions, the extent of charge separation is greater and the species velocity is greatly driven by electric body force (*qE)* as represented by this approximation The following Poisson equation is used to calculate the potential drop.

$$\frac{\partial^2\varphi}{\partial x^2} = -\frac{e}{\varepsilon}(n_i - n_e) \tag{37}$$

Equation 37 is rather interesting as it possesses no time derivatives, yet temporal behavior is nontrivial. Inserting Equation 32 into 37 and integrating on *x* gives the following current balance:

$$\varepsilon\frac{\partial^2\varphi}{\partial x\partial t} = en_iV_i - en_eV_e + I(t) \tag{38}$$

where the constant of integration, $I(t)$, is the total current density. It may be noted that the effect of varying speed of ionization on the rate of species production is indirectly reflected on the net current density. Equation 38 completes the dynamic system of equation and serves as a means to calculate electrode potential from conservation principle. A simple discretization for the boundary element (assuming that the mesh is fine enough to validate the linear approximation) yields the following:

$$\varepsilon \frac{\left(\varphi_n^t - \varphi_n^{t-1}\right) - \left(\varphi_{n-1}^t - \varphi_{n-1}^{t-1}\right)}{\Delta x \Delta t} = e\left(n_i V_i\right)_n^t - e\left(n_e V_e\right)_n^t + I(t) \tag{39}$$

where n and (n-1) are the two boundary nodes and t is the time. Hence the solution can be iterated on the boundary condition (within a given timestep) to update the electrode potential.

The finite element weak statement for Equations 34 and 36 in conjunction with Equation 32 is written as

$$S_e \left(\begin{array}{l} \int_\Omega \mu_i E \psi \frac{d\psi^T}{dx} dx\{N_i\}_e + \int_\Omega \psi \psi^T \mu_i \frac{d^2\varphi}{dx^2} dx\{N_i\}_e \\ + \int_\Omega D_i \frac{d\psi}{dx} \frac{d\psi^T}{dx} dx\{N_i\}_e - \int_{\partial\Omega} D_i \psi \left[\frac{dN_i}{dx}\right] dx - \int_\Omega S \psi \psi^T dx\{N_e\}_e \end{array} \right)_e = F_{N_i} \tag{40}$$

$$S_e \left(\begin{array}{l} -\int_\Omega \mu_e E \psi \frac{d\psi^T}{dx} dx\{N_e\}_e - \int_\Omega \psi \psi^T \mu_e \frac{d^2\varphi}{dx^2} dx\{N_e\}_e \\ + \int_\Omega D_e \frac{d\psi}{dx} \frac{d\psi^T}{dx} dx\{N_e\}_e - \int_{\partial\Omega} D_e \psi \left[\frac{dN_e}{dx}\right] dx - \int_\Omega S \psi \psi^T dx\{N_e\}_e \end{array} \right)_e = F_{N_e} \tag{41}$$

The sheath edge is identified as the ion attains the modified Bohm velocity based on G-S relation (Godyak and Sternberg, 1990) as $V_B[1+c]^{-0.5}$ where the collision parameter $c = 0.5\pi\lambda_{De} / \lambda_i$ and λ_i(cm) ~1/330p.

Boundary conditions

The left electrode is grounded, $\varphi(0) = 0$, and a sinusoidal rf potential $\varphi_{rf} = \varphi_{rms} \sin 2\pi f t$ with φ_{rms}=100V and f=13.56 MHz is applied to the right electrode through the capacitor (C = 0.1) where $\partial\varphi(2)/\partial t = I(t)/\mathrm{C}$, and φ may be related to total current through Equation 38 thereby completing the circuit in Figure 11.

The electron flux at both electrodes is based on the electron thermal velocity ($V_{e,th}$) whose magnitude is given by $\Gamma_e = n_e V_{e,th}/4$ and is directed towards the wall. For case A, we utilize the collisionless model and employ Boltzmanian electron distribution at the wall. Hence the flux becomes:

$$\Gamma_e = n_e \sqrt{\frac{T_e}{2\pi m_e}} = n_e^{|z_w - \Delta z|} \sqrt{\frac{T_e}{2\pi m_e}} e^{-\Delta\phi} \tag{42}$$

Homogeneous Neumann boundary condition ($\partial n_i/\partial x=0$) is imposed for ions at both electrodes. The domain is discretized into 400 elements and ψ is interpolated using a linear basis function. We used the convergence criterion for all variables at any iteration as 10^{-3}.

Results and discussion

Case I: Collisionless Discharge

Figure 12 shows the computed rf discharge characteristics for a collisionless sheath at applied frequency $\omega << \omega_{pe}$. The discharge gets established due to external power supply in form of a sinusoidal wave at the right electrode. The inherent difference between ion and electron inertia is one fundamental concept, governing the discharge. The direction and magnitude of the electric field is based on the space charge separation. The spatio-temporal evolution of ϕ and E in Figure 12(a) and Figure 12(b) match well with those published in literature (Lieberman and Lichtenberg, 1994 & Raizer et. al., 1995). It is interesting to note that the slope of E is always positive for most of the simulation domain and near the powered electrode the magnitude always remains positive. This indicates the dc bias of the potential. Figure 12(c) gives an approximate

indication of sheath edge location at which space charge separation become prominent as the ion and electron density curves bifurcate.

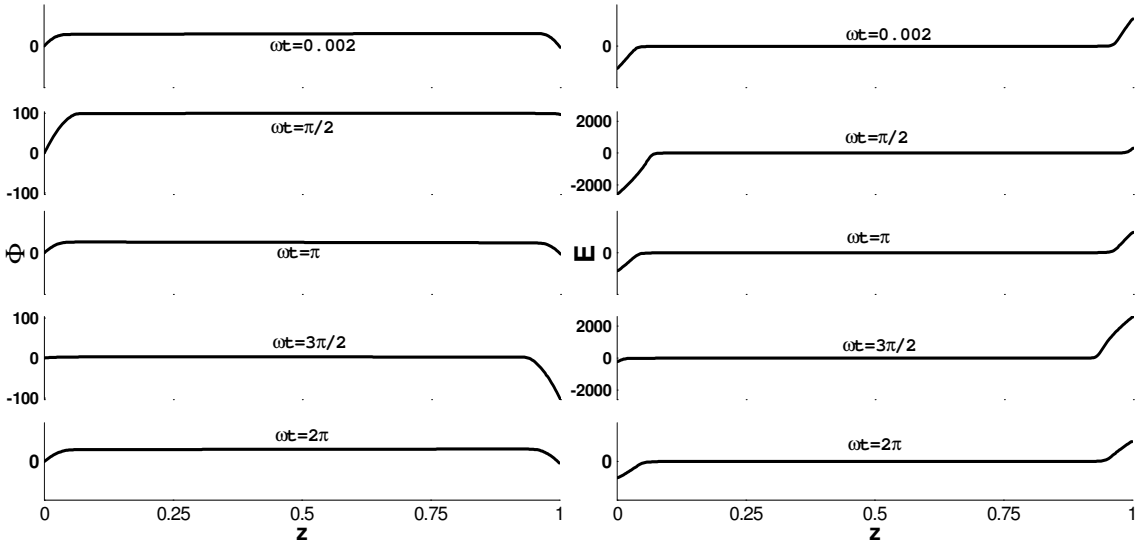

(a) (b)

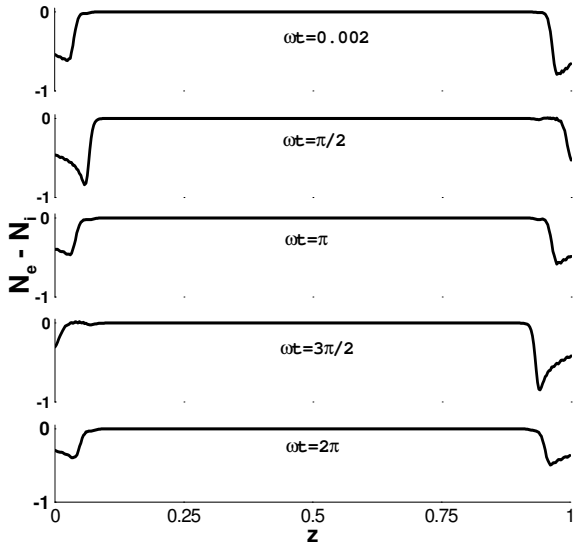

(c)

Figure 12. Variation of (a) potential (b) electric field and (c) charge separation at various instants of the rf cycle.

Case II: Collisional Discharge

Figures 13-15 illustrate the computed rf discharge characteristics for the collisional model. The time-averaged values of potential and electric field for one rf cycle are shown in Figure 13. The average potential of one cycle has been compared to the potential in Figure 13(a) when it reaches its maximum value at $\pi/2$. The average discharge potential is ~40% of the peak potential. Also notice that plasma potential (in the bulk) is always positive and vanishes to zero potential at the electrodes. Hence this also explains the positive nature of the space charge sheath formed. The time-averaged electric field in the domain for one rf cycle is shown in Figure 13(b). In the bulk plasma, the field cancels out in opposing half of applied potential and hence there is not net force on the charged particles. The direction of the field, as mentioned before is always pointed towards the electrode.

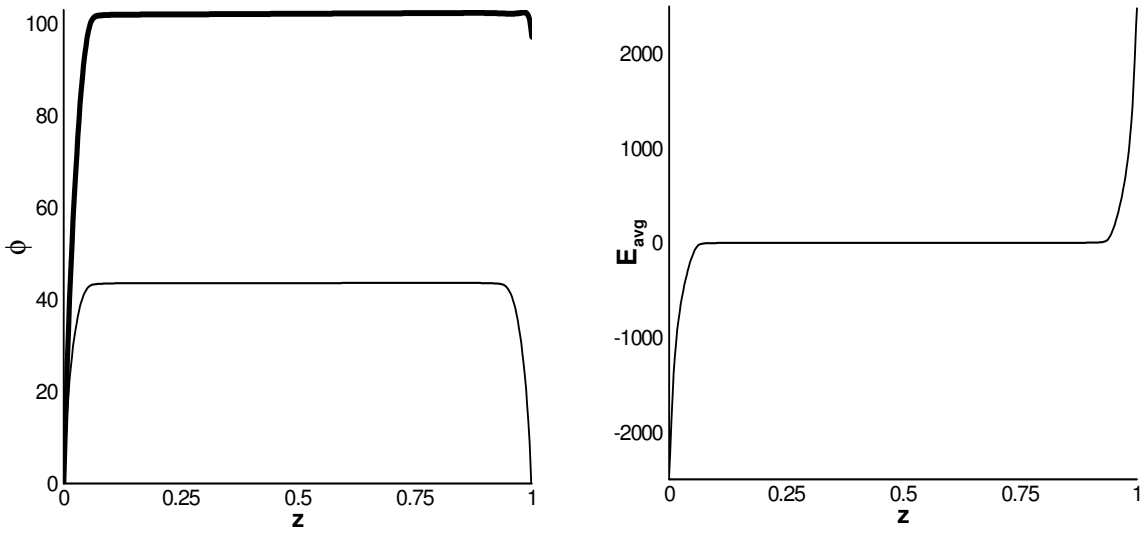

(a) (b)

Figure 13. (a) Time averaged (thin line) and peak potential at $\pi/2$ (thick line) and (b) time averaged electric field.

The flooding and receding of the electron gas, exposing the immobile ions to the electrode (periodically) at every $k\pi$ radians is shown in Figure 14(a). There is an increase of electron density at the electrode momentarily collapsing the electron sheath, which is otherwise inevitable. This energy is imparted to the electrons through accelerating fields. The electrons thus oscillate about the center of the domain driven by the potential difference across the electrodes.

Figure 14(b) shows the extent of deviation of plasma from quasi-neutrality in the presence of electrodes. In case A, ions are collisionless inside the sheath; and to preserve the flux, they gradually decay to a non-zero value. In case B, ions experience more than one ionizing collisions inside sheath. Unlike case A, there is no clear sheath edge boundary due to the presence of collisions. The magnitude of charge separation is greater in case B than in case A also attributed to the ionization in the sheath. The spatial evolution of net charge in the domain differs between cases A and B, particularly in the plasma-sheath edge. For example, as we move from the bulk plasma to sheath, there is a sharp drop in electron density (due to high cathode potential) and the sheath is almost devoid of electrons near grounded electrode at $\pi/2$.

The profiles of potential and electric fields for collisional discharge are similar to case A except for higher magnitudes of E induced in the sheath for case B. The electric field in the bulk plasma is observed to be a periodic function in the timescale of the applied frequency as $E(\tau) \approx 3\cos(\pi+\tau)$. The phenomenon is noticeable near an electrode in the positive half of applied potential (at $\pi/2$) and occurs at relatively weak electric fields. Ions, due to their high inertia, hardly respond to the weak fields in the bulk plasma. This is not true inside sheath. The highly oscillating fields exert high electrostatic force

on the ions and they enter the sheath with high velocities. The timescales of ions and applied frequency are comparable for this plasma density and plasma frequency.

Figure 14(d) shows the electron heating ($\boldsymbol{\Gamma}(\tau).\mathbf{E}(\tau)$) profile. It is evident that electrons are periodically heated and cooled corresponding to the sheath oscillation and hence the electron energy increases or decreases accordingly. The effect of electrical double layer amplifying the electron heating near sheath edge is also noticed. Sheath heating is a dominant phenomenon in radio frequency driven discharges.

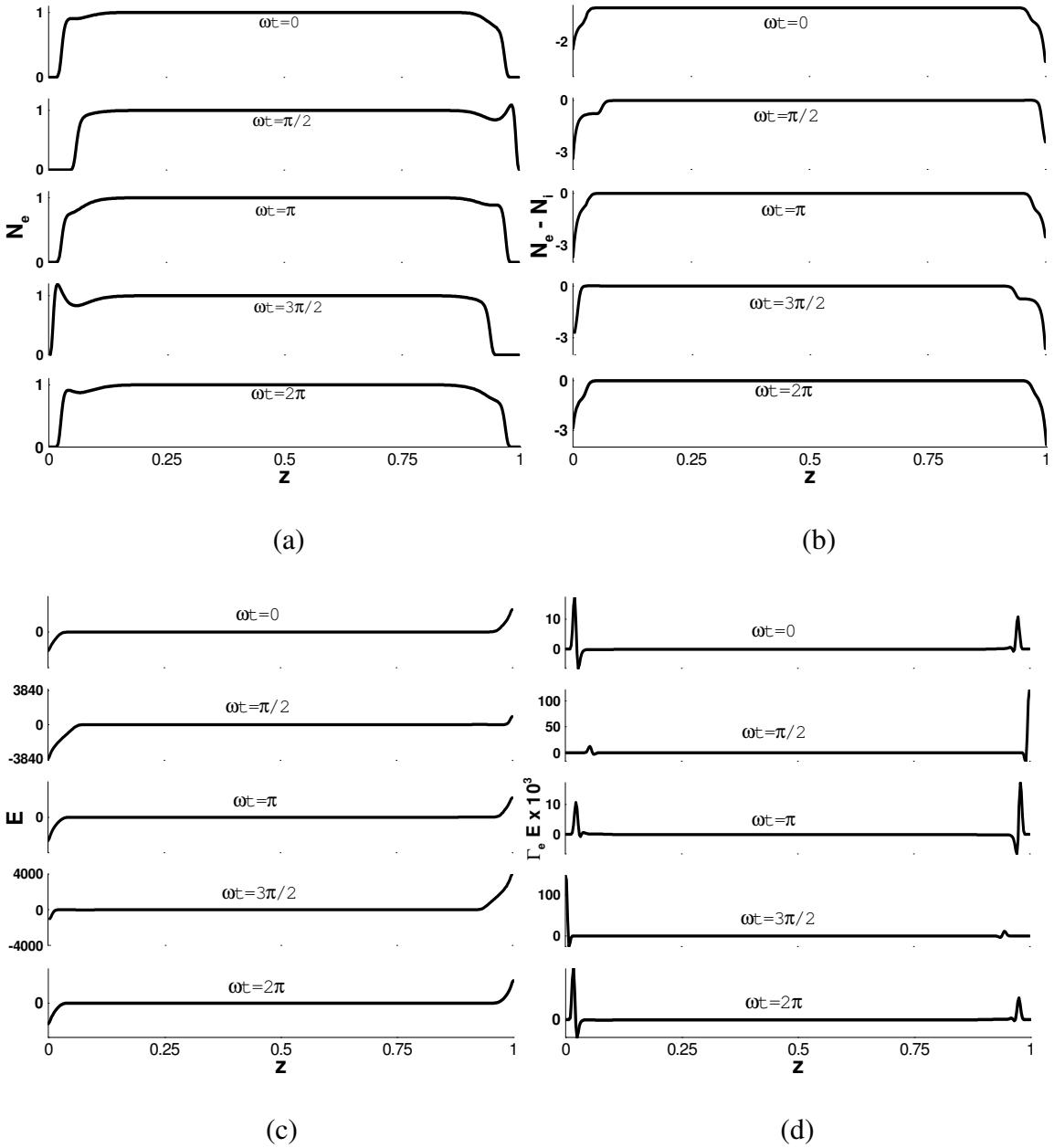

Figure 14. Variation of (a) electron number density (b) charge separation (c) electric field and (d) electron heating at various time stations of the rf cycle.

The electron flux in the bulk is estimated to vary as $N_e u_e \approx 28 \cos\tau$. Electrons, being lighter get transported across the domain in response to the applied potential. Due to their high mobility, the effect of double layer is amplified causing a local fluctuation near the sheath edge (e. g at $\pi/2$) which gets reflected in $N_e u_e$ causing a local fluctuation

as seen in Figure 15(a). The variation of total current at the powered electrode for three cycles of applied potential is reported in Figure 15(b). The total current is conserved in space at any particular moment. It should be noted that the displacement current and conduction (electron and ion) current magnitudes are comparable at the subject pressure of 0.1 torr. The peak of the total current is observed at every $(4k+1)\pi/2$. A minor secondary peak is also observed in Figure 15(b) at the instant when the applied potential switches direction on the electrode. It is also noted that this secondary current peak is less significant for lower ionization rates.

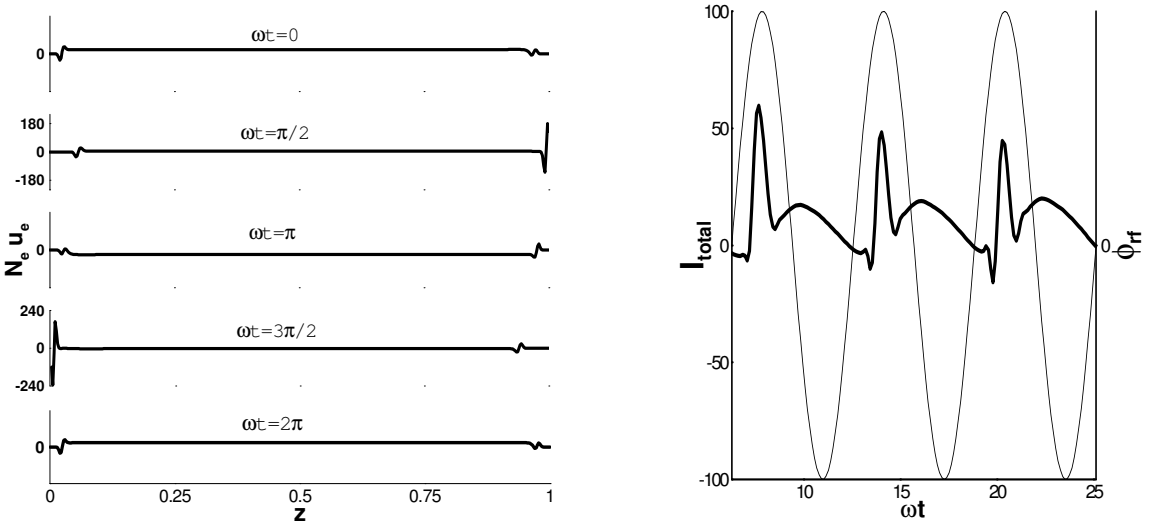

(a) (b)

Figure 15. (a) Spatio-temporal variation of electron flux and (b) temporal evolution of wall potential (thin solid line) and total current (dark solid line).

The difference in normalized sheath thickness at the grounded left electrode (z_L) and the powered right electrode ($1-z_R$) shows an expected 2π periodicity between the points of extremum sheath locations with a phase lag of π radians. The oscillation of

sheath width z_w is plotted in Figure 16 using the G-S relation stated in Sec. II. Based on curve fitting with an estimation error of ~4%, we correlate the sheath thickness as $z_w \approx 0.04 \pm 0.03 \sin \tau$. For the discharge at 0.1 torr, the simulation results predict the maximum sheath width $z_{w\text{-}max} \sim 20\ \lambda_{De}$, which agrees with the available literature (Lieberman and Lichtenberg, 1994). The sheath accounts for nearly 80 % potential drop for one rf cycle. The average sheath thickness was numerically found to be higher for a collisionless sheath under similar conditions than a collisional one.

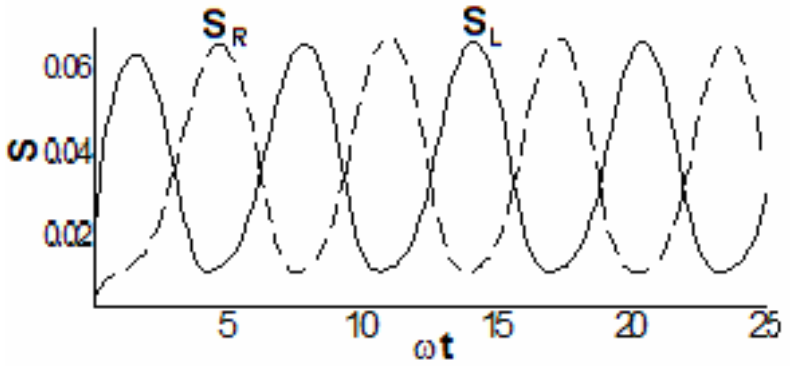

Figure 16. Temporal evolution of left ($S_w=z_L$) and right ($S_w=1-z_R$) sheath width.

IV. MODELING OF TWO DIMENSIONAL DISCHARGES

The increasing application of plasma in aerospace community demands supporting theories to quantify and explain experimental observations. Particularly, with growing interest in plasma based flow control techniques, there is a necessity to estimate the plasma discharge characteristics effectively. A time accurate and geometry versatile numerical tool would prove useful in accurately calculating the discharge characteristics and predicting its electrodynamic structure. This chapter is focused towards modeling and simulation of a two-dimensional plasma discharge formed in the high frequency, low-pressure regime.

When the lateral extent of a discharge becomes comparable to the transverse stretch in presence of geometric or electrical inhomogeneities, the sheath becomes multi-dimensional and a one-dimensional model is not sufficient to capture the required features. Specifically, the interest to model the effect of magnetic field necessitates a higher dimensional consideration.

The dynamics of sheath in one dimension in the low and intermediate pressure regime have been studied in literature from numerical simulations. Boeuf and Pitchford (1995), Dalvie (1993) et. al and Passchier and Godheer (1993) simulated argon discharge for cylindrical geometry in two-dimension. Most of these cylindrical configurations are related to Gaseous Electronics Conference Reference cell which serves as a common

platform for experimental and modeling studies and a well-characterized system in which fundamental studies of plasma behavior can be conducted. Kim and Economou (2003) investigated plasma formation over an inhomogeneous flat wall. In these simulations, fluid and/or PIC treatments were used to model the system.

Recent efforts have considered effect of external electromagnetic force on plasma wall interaction (Kim and Economou, 2003 & Hou et. al., 2004). Inspite of these earlier attempts, the capability to simulate characteristics of a discharge in the presence of electric and magnetic fields remain limited.

We present a hydrodynamic plasma model in two-dimension configurations under applied electric and magnetic fields. The axial and transverse nature of resulting electrostatic field, forces and potential are investigated. The MIG code employs a self-consistent approach to model the rf induced plasma interactions.

Problem Specification

The unsteady transport for electrons and ions are derived from fluid dynamics in the form of mass and momentum conservation equations. The species momentum is modeled by the drift-diffusion equation under isothermal conditions. Here, the flux is written in terms of species transport coefficients by neglecting inertial acceleration in the collisional regime. Electron temperature (T_e) is of the order of 1 eV (~11,600K) and ions are assumed cold at 0.026 eV (~300 K). The continuity equation for ion and electron number densities is given by:

$$\frac{\partial n_i}{\partial t} + \nabla.(n_i \mathbf{V}_i) = \alpha \left|\Gamma_e\right|$$
$$\frac{\partial n_e}{\partial t} + \nabla.(n_e \mathbf{V}_i) = \alpha \left|\Gamma_e\right| \qquad \left|\Gamma_e\right| = \sqrt{\left(n_e V_e\right)_x^2 + \left(n_e V_e\right)_y^2} \tag{43}$$

where *n* is the number density and *V* is the species hydrodynamic velocity. As the sheath is collision dominated, electrons are not assumed to follow Boltzmannian distribution. For a pressure of 0.1 Torr, electron-ion recombination ~$2\text{x}10^{-12}$ cm^3/s and has negligible effect on the mass balance (Boeuf and Pitchford, 1995). The discharge is maintained using a Townsend ionization scheme resulting in production of charge through impact ionization. The ionization rate is usually expressed as function of electron drift velocity and Townsend coefficient (Boeuf and Pitchford, 1995). The Townsend coefficient, α appearing in Equation 43 is given by:

$$\alpha = Ape^{-B/(|\boldsymbol{E}|/p)} \tag{44}$$

where $A = 34\ \text{cm}^{-1}.\text{Torr}^{-1}$ *and* $B = 16\ [\text{V}/(\text{cm}.\text{Torr})]^{0.4}$ are pre-exponential and exponential constants, respectively. $|\Gamma_e|$ is the effective electron flux which varies spatially and mainly depends on the electric field. The electronic and ionic flux in Equation 43 is written as:

$$n_e\boldsymbol{V}_e = -n_e\mu_e(\boldsymbol{E}+\boldsymbol{V}_e\times\boldsymbol{B}_z) - D_e\nabla n_e \tag{45}$$

$$n_i\boldsymbol{V}_i = n_i\mu_i(\boldsymbol{E}+\boldsymbol{V}_i\times\boldsymbol{B}_z) - D_i\nabla n_i \tag{46}$$

where E is electrostatic field given by $\boldsymbol{E}=-\nabla\varphi$ is the electric field. $\boldsymbol{V}$x$\boldsymbol{B}$ is the Lorentz force term due to presence of magnetic field. The magnetic field is acting only along the z-direction; $\boldsymbol{B}=\{0,0,B_z\}$.

Since Equations 45 and 46 are of 0^{th} order, the bandwidth of the problem can be considerably reduced by substituting into Equation 43. The substitution gives rise to convection-diffusion type equation, which apart from being more stable increase computational efficiency. Hence:

$$\frac{\partial n_i}{\partial t}+\frac{\partial}{\partial x}\left\{b_i\left(n_i\mu_i\left(E_x+\beta_i E_y\right)-D_i\frac{\partial n_i}{\partial x}\right)\right\}$$
$$+\frac{\partial}{\partial y}\left\{b_i\left(n_i\mu_i\left(E_y-\beta_i E_x\right)-D_i\frac{\partial n_i}{\partial y}\right)\right\}=\alpha\left|\Gamma_e\right| \quad (47)$$

$$\frac{\partial n_e}{\partial t}+\frac{\partial}{\partial x}\left\{b_e\left(n_e\mu_e\left(E_x+\beta_e E_y\right)-D_e\frac{\partial n_e}{\partial x}\right)\right\}$$
$$+\frac{\partial}{\partial y}\left\{b_e\left(n_e\mu_e\left(E_y-\beta_e E_x\right)-D_e\frac{\partial n_e}{\partial y}\right)\right\}=\alpha\left|\Gamma_e\right| \quad (48)$$

After some algebraic manipulation, we end up in the following equations,

$$\frac{\partial n_i}{\partial t}+b_i\left[\nabla.\left(n_i\mathrm{V}_i\right)_{B=0}-\mu_i^2 B\left\|J_{xy}\left(n_i,\varphi\right)\right\|\right]=\alpha\left|\Gamma_e\right| \quad (49)$$

$$\frac{\partial n_e}{\partial t}+b_e\left[\nabla.\left(n_e\mathrm{V}_e\right)_{B=0}-\mu_e^2 B_z\left\|J_{xy}(n_e,\varphi)\right\|\right]=\alpha\left|\Gamma_e\right| \quad (50)$$

Here $b_i(=1/1+\beta_i^2)$ and $b_e(=1/1+\beta_e^2)$ are functions of hall parameter (β_i and β_e) and J is the Jacobian determinant involving partial derivatives of n and φ.

The effect of magnetic field on the discharge is theoretically brought into the system through introduction of an additional expression involving mobility, as seen from Equations 49 and 50. The convective term ($\nabla.n\mu E$) gets altered accordingly in the *x* and *y* directions. This affects the electric field-number density coupling resulting in transfer of momentum between axes. An appropriate choice of B magnitude and direction can accordingly increase or decrease the stream wise momentum through electrostatic forces. Modification in discharge characteristics is expected in a direction perpendicular to the significant axis of the problem.

The electron mobility μ_e in Equation 48 is given by $\mu_e = 3\times10^6 cm^2V^{-1}s^{-1}$, at *pd* = 0.2 Torr.cm. The electron diffusion coefficient, D_e is calculated from the Einstein relation $D_e = kT_e/e\mu_e$. The ion diffusion coefficient is $D_i = 200\,cm^2/s$ at 300K. The ion mobility μ_i is expressed as a function of reduced field *(E/p)* as before.

The relation between electrostatic field and charge separation is given by the Poisson equation:

$$\varepsilon\nabla.\boldsymbol{E} = -e(n_e - n_i) \tag{51}$$

The electrodes are assumed to be fully absorbing. Secondary Electron Emission (SEE) can be neglected for pressure of 0.1 Torr in Argon; as low as <<1% of secondary electrons are emitted back at the electrode. For all the cases considered, *d*=2 cm, $\omega/2\pi$=13.56 MHz and the reference density $n_0=2\times10^{15}$ m^{-3}.

The finite element weak statement for Equation 47 is given in Equation 52. The introduction of magnetic field makes the formulation look complicated and cumbersome. Thought the underlying weak formulation is the same and simple to use once a framework has been developed. For example, the weak statement for Equation 47 is as follows:

$$\frac{\partial n_i}{\partial t} + S_e \left(\begin{array}{l} \int_\Omega \mu_i \left(E_x + \beta_i E_y\right)\psi \frac{d\psi^T}{dx} dx\{N_i\}_e + \int_\Omega \mu_i \left(E_y - \beta_i E_x\right)\psi \frac{d\psi^T}{dy} dy\{N_i\}_e \\ + \int_\Omega \mu_i \nabla^2\varphi\psi\psi^T dx\{N_i\}_e + \int_\Omega D_i \frac{d\psi}{dx}\frac{d\psi^T}{dx} dx\{N_i\}_e + \int_\Omega D_i \frac{d\psi}{dy}\frac{d\psi^T}{dy} dy\{N_i\}_e \\ - \int_{\partial\Omega} \psi\left[\frac{dN_i}{dx}\right] dx - \int_{\partial\Omega} \psi\left[\frac{dN_i}{dy}\right] dy - \int_\Omega S\psi\psi^T d\tau\{N_e\}_e \end{array} \right)_e = F_{N_i} \tag{52}$$

The weak statement for electrons and potential may be written in the same way. The system utilizes a Sub-Grid eMbedded algorithm (SGM) (Roy and Baker, 1998) which ensures a node-wise monotone solution. The SGM is incorporated to the dissipative flux terms that are altered suitably based on local cell velocity and thus is expected to ensure a minimum dispersion error.

Results and Discussion

Case I: Benchmark Case

The two-dimensional formulation was tested to plasma formed between two symmetric electrodes for a Direct current glow discharge using nitrogen. The geometry and discharge conditions correspond to Surzhikov and Shang (2004). The computational grid consists of 25 × 30 bi-quadratic (9 nodes) finite elements. An electrode potential of 533 V is applied through an external circuit with resistance 300kΩ driven by an electromotive force of 2000 V. The model does not neglect diffusion in x and y directions for the entire domain including plasma and sheath.

The cathode is at y=0 while y=2 cm is the anode. Vanishing ion density is imposed at anode while the electrons at cathode are calculated using flux balance using a secondary emission coefficient (=0.1). The left and right boundaries of the computational domain are maintained at symmetric conditions. Electrons and ions are localized to center of the geometry along x-axis based on initial condition and was calculated based on a pre-estimated cathode layer thickness and current column length (Surzhikov and Shang, 2004).

The results of the simulation at pressure of 5 torr in the absence of magnetic field are presented. Figures 17(a) and 17(b) show the lines of constant electric potential and

ion density. The potential in previous simulation by Surzhikov and Shang (2004) are also shown for comparison. The potential lines bend towards the cathode. This gives rise to high electric field (directed towards electrode) driving electrons away forming ~7.5 % thick cathode layer. The ion density near cathode rises to an order of magnitude higher than that near center of discharge and indicates a qualitative similarity. When a magnetic field of 0.01 Tesla is applied, the ion density gets shifted in the axial direction along the electrode surface (Figure 17(c)). A widening of discharge near cathode is also observed. The direction of drift depends on direction of magnetic filed lines while the magnitude of shift of iso-lines depends on value of determinant of Equations 49 and 50.

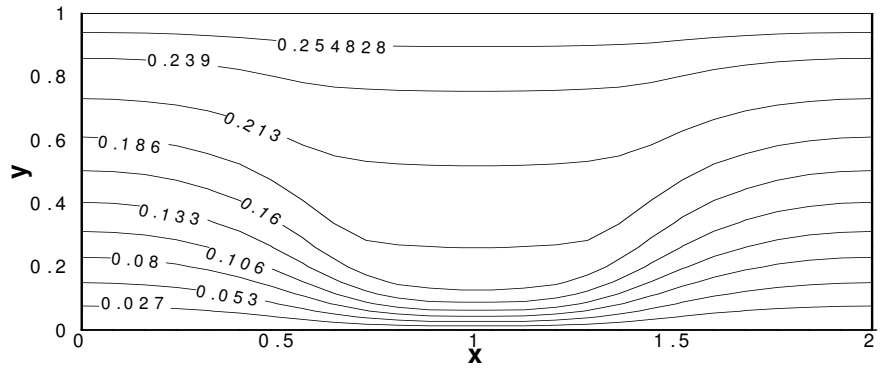

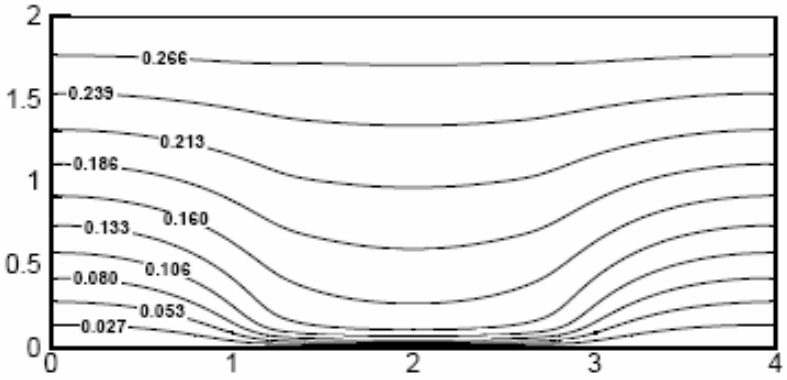

(a)

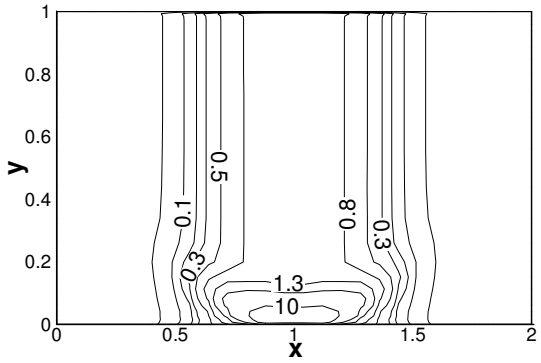

(b)

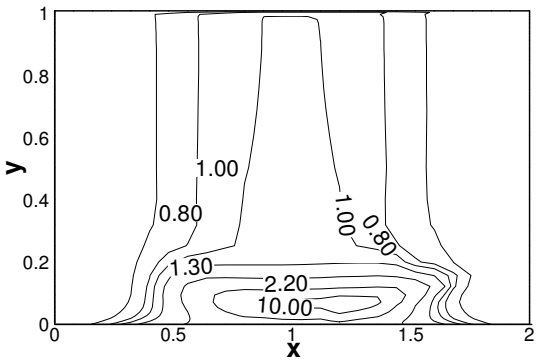

(c)

Figure 17. (a) Electric potential contour comparison between present simulation and reported simulation (Surzhikov and Shang, 2004) and (b) ion density contours for B=0 and (c) ion density contours for B=0.01 T. All results shown here are for Nitrogen gas at 5 Torr.

The calibrated formulation is applied to model plasma of a pure argon gas discharge. The schematic model and the computational domain are shown in Figure 18. The electrode is ~2 cm long and is located ~1 cm from left boundary. The top surface is considered quasi neutral. This assumption is valid as the height of domain chosen is much greater than Debye length. A height of $\sim 200\lambda_{De}$ is chosen for present case. The electrodes are assumed to have a negligible thickness compared to significant dimensions of the model and are presently ignored for simplicity.

The computational grid (Figure 18) consists of 25 × 20 biased bi-quadratic finite elements with the first node ~0.01 cm from wall. The maximum aspect ratio is about 6 for elements near the wall and is close to one far away from electrode. This is a trade-off between computational time and near-wall mesh resolution. The presence of mm scale sheath necessitates mesh refinement close to wall. This increases the aspect ratio of elements near the wall which has to be compensated by increasing stream-wise elements at the cost of computational time. In the absence of magnetic field, the discharge may be treated as symmetric about x=1. Similar geometry has been treated recently in literature (Kim and Economou, 2003) for quiescent and fluctuating argon plasmas in the collisionless low-pressure regime. Apart from being a more realistic configuration that brings edge effects into consideration, the importance of understanding this discharge configuration proves useful in plasma based flow control application that is being widely investigated as a means to alter near wall boundary layer profile. A recent investigation studied the effect of plasma on neutral gas flow in an asymmetric configuration for a Dielectric Barrier Discharge (DBD) (Roy, 2005). Hence this formulation provides a

framework, which can be built upon to study high-pressure discharges and effect of magnetic field interaction in collision-dominated sheath.

As can be observed from Figure 18, there is a net flow of current into the metallic wall, while the current path is almost parallel at dielectric surface. This gives rise to a near wall inhomogeneity in the model, which might be compared to a mathematical discontinuity. This inherent feature introduces considerable numerical difficulty at the electrode-insulator edge. Maximum plasma generation is limited to this region which when not properly handled may affect numerical stability. As mentioned earlier, artificial stabilization techniques like SGM have been implemented to minimize dispersion error and ensure a node wise monotone solution.

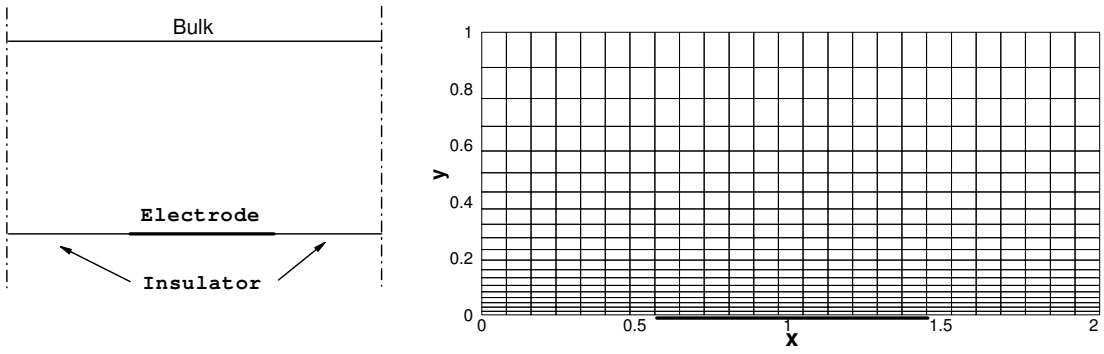

Figure 18. Schematic of a perfectly flat electrode-insulator configuration and computational grid.

The system of Equation 47-48 and 51 are solved using the following boundary conditions. The electron flux imposed at electrode is based on the electron thermal velocity and directed towards the electrode. $(N_eV_e)_Y$ to electrode is 0 if drift velocity is away from electrode. Boundary condition (at electrodes) for ions is imposed homogeneous Neumann ($\partial N_i/\partial n=0$). The normal current of charge carriers is nullified at

insulator boundary. In the left and right boundary, the slopes $\partial N_i/\partial x=0$, $\partial N_e/\partial x=0$ and $\partial \phi/\partial x=0$ are ensured.

Case II: Steady State Discharge in Presence and Absence of Magnetic Field

A steady state discharge is first studied for an applied voltage of -50V on the exposed electrode. Figure 19(a) shows iso-lines of electric potential for a cathode potential of –50V at steady state. The symmetric nature of the contour in the absence of magnetic field about x=1 may be noted. Figures 19(b), 19(c) and 19(d) compare the axial distribution of potential, electron number density and charge difference at two different y locations, close to and away from the bottom plate. Due to large difference of potential between top boundary and electrode, the variation of characteristic is felt in y-axis. Hence the magnetic field strongly affects the stream-wise distribution because of heavy y-momentum transfer into *x*-direction (as seen from Equation 47 and 48). The solid line shows the variation in absence of magnetic field while the dotted line is for a low magnetic field intensity of five Gauss. The sharp change of characteristics (for example, spike like pattern for electron number density) near the electrode-insulator edge is expected. Most of the plasma formation is limited to this region. As shown in Figure 19(b), the insulator is less cathodic (~25*V* difference than cathode potential) and behaves like a pseudo-anode collecting electrons. Corresponding to this pseudo-electrode, a sharp increase in electron density is observed near the highly depleted cathode sheath layer. In the presence of magnetic field, the potential lines (for example, near right electrode-insulator edge) are modified along the electrode surface. They are shifted from its initial position towards the right. This change is reflected in the charged species (theoretically

through the Poisson equation) causing a variation in charge separation. Hence, the analysis qualitatively shows effect of magnetic field on discharge characteristics.

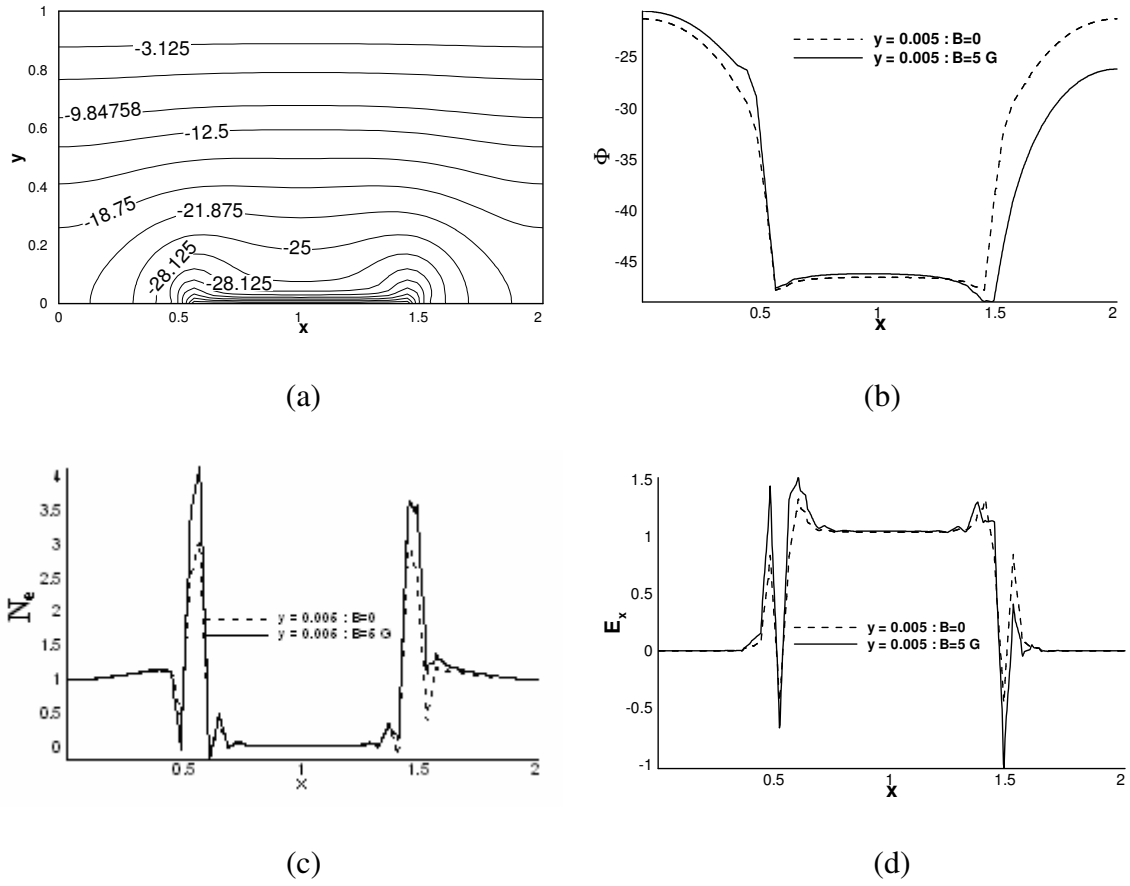

Figure 19. Steady state discharge (a) electric potential contour for B=0 (b) variation of potential (c) variation of electron number density and (d) variation of axial electric field at two *y* locations in the presence and absence of magnetic field. All results shown here are for Argon at 0.1 Torr.

Case III: rf Discharge in the Presence and Absence of Magnetic Field

The steady state discharge in case II was analyzed for fairly low magnetic field intensity. With the gained theoretical understanding of electromagnetic interactions, a transient plasma discharge is simulated for a higher magnetic field of 20 Gauss in the presence of an oscillating potential with a peak-to-peak of 100 volts. In order to

understand the variation of plasma characteristics in the presence of magnetic field, the solution is compared with a simulation without magnetic field, all other conditions being the same.

Figure 20(a) and 20(b) show the progress of solution in terms of the residual and solution norm, respectively evolving with time expressed in radians. As can be seen, the solution norm has reached a steady state or a harmonic periodicity as can be seen from peaks of the second and third cycle. A typical solution takes about 2.43 sec (CPU time) for assembly and 2.5 sec for solver per iteration and a normal timestep takes four to six iterations to converge.

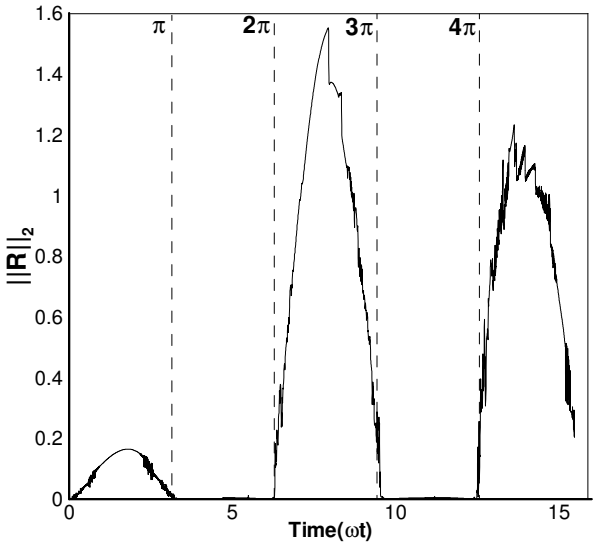

(a)

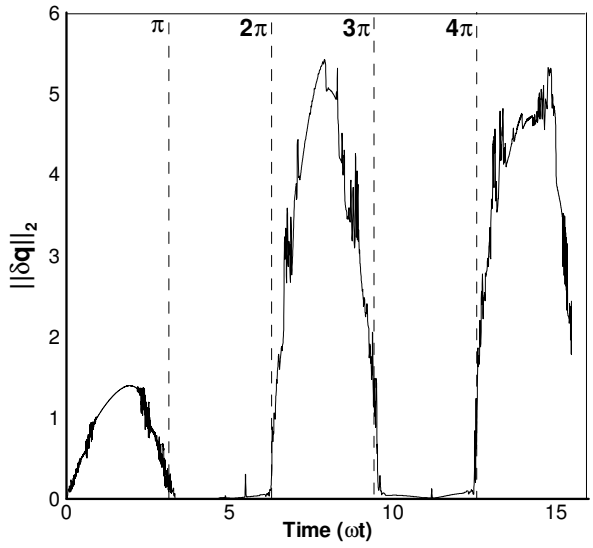

(b)

Figure 20. L_2 norm of (a) residual and (b) increment in solution

The stream-wise and transverse variations at different locations are shown in Figures 21(a) to 21(c). It was observed in the simulation that except for localized regions

near the electrode-insulator edge, the magnetic field had less pronounced effect on the transverse solution characteristic relative to stream-wise components.

The potential lines are symmetric at all four times of the cycle plotted. At $\pi/2$, the electrode is highly cathodic and a sheath starts forming with a large change of potential across a few millimeters away from the electrode. Near the electrode-insulator edge, the lines wrap around the corners resulting in semi-circular patterns. Due to axial and transverse extent of discharge, there are instantaneous pseudo-anodes that are formed and most of electron accumulation (not shown) is limited to the edge. When the applied potential shifts direction, the electrons start responding first to the rise in potential. The net potential is affected by space charge accumulated in pseudo-anodes from the negative cycle. During positive peak of the cycle, the potential lines do not wrap around the edge as was observed during the negative stroke. The formation of instantaneous electrodes near real anode and cathode causes this delay.

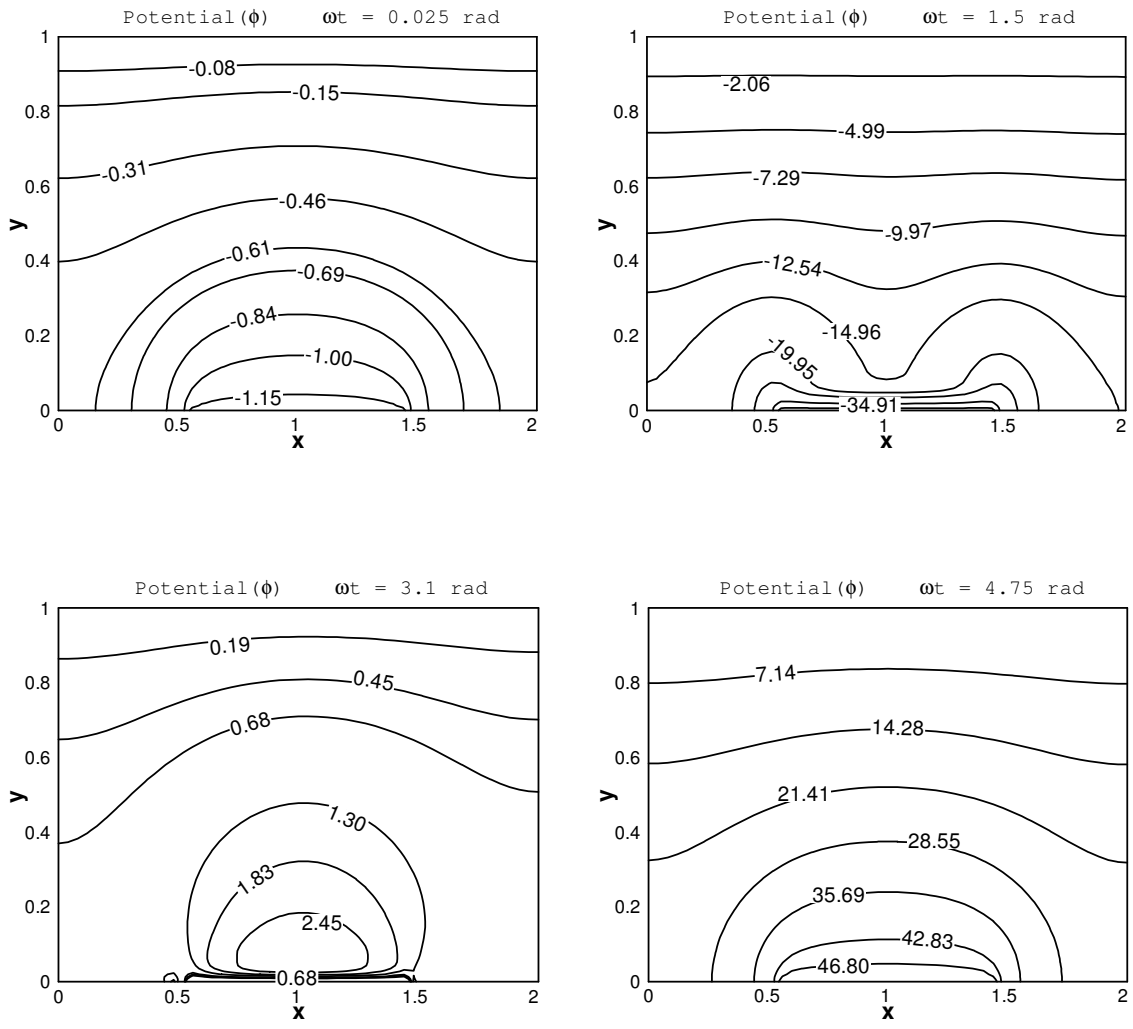

Figure 21. Electric potential at four different times of rf cycle without magnetic field.

Figure 22 shows the potential variation under the effect of external applied magnetic field of 20 gauss. The symmetry of the discharge about x=1 is affected and profile is shifted to the right as can be seen at $\pi/2$ radians. This brings about a change in near wall charge distribution and electrostatic fields. The **V×B** component force visibly pushes the field line to the right reducing the near curving of the constant potential lines near the left edge. At π radians, plasma distortion due to applied magnetic field is less intense. Interestingly at $3\pi/2$, the potential closely resembles a zero magnetic field case.

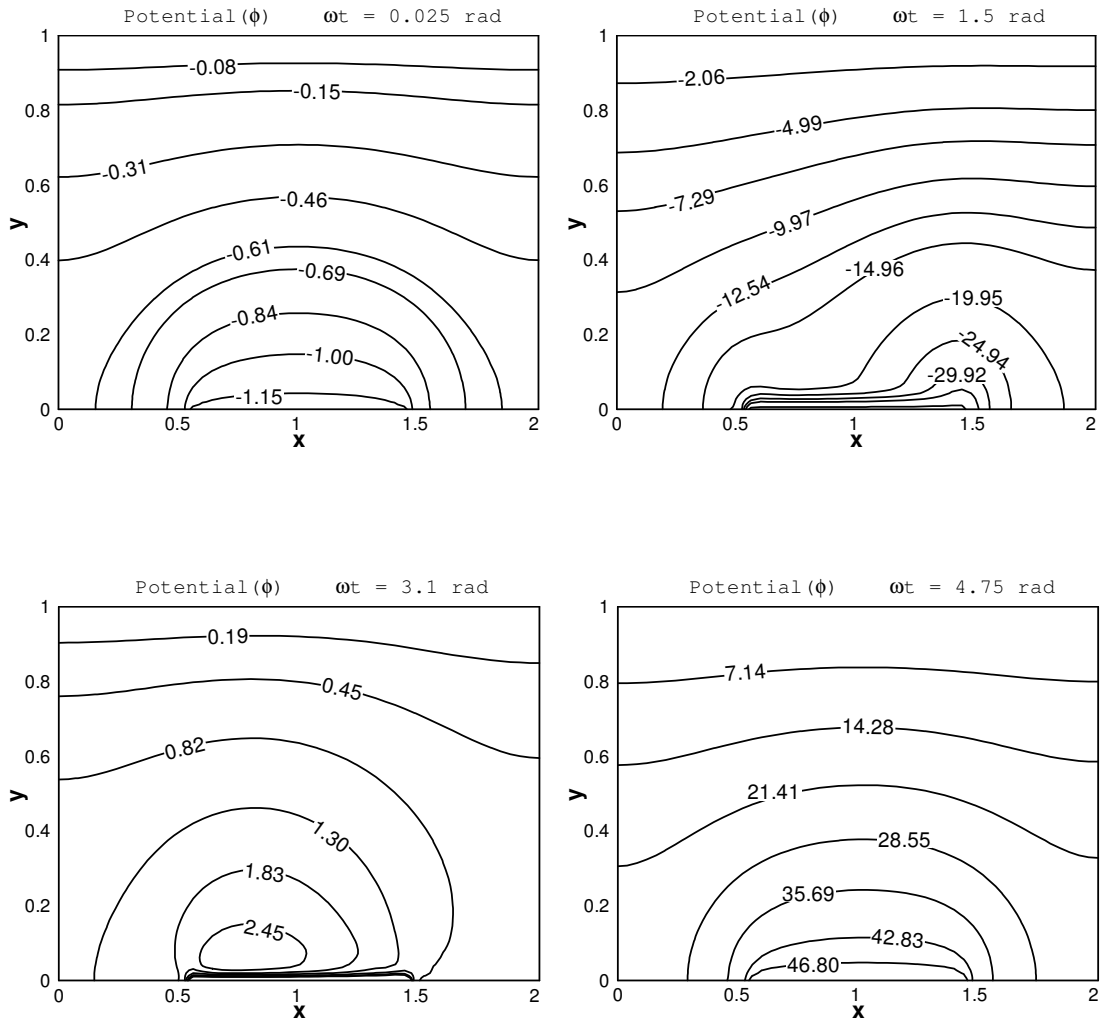

Figure 22. Electric potential at four different times of rf cycle with magnetic field.

Figure 23 plots variation of electric field close to the electrode at four times of the rf cycle. This spatio-temporal evolution may be of much value in flow control applications where electrostatic force is considered as one possible mechanism of momentum transfer from plasma to background neutral gas. Due to the nature of the geometry, the potential across the right and left edge changes sign. This is obvious from the peaks of field near 0.5 and 1.5. For example, the stream-wise field varies between normalized values of 175 and –175 in the absence of magnetic field at $\pi/2$. On the other

hand, the observed field in nearly ~42.8% higher in the presence of an additional magnetic force on the species.

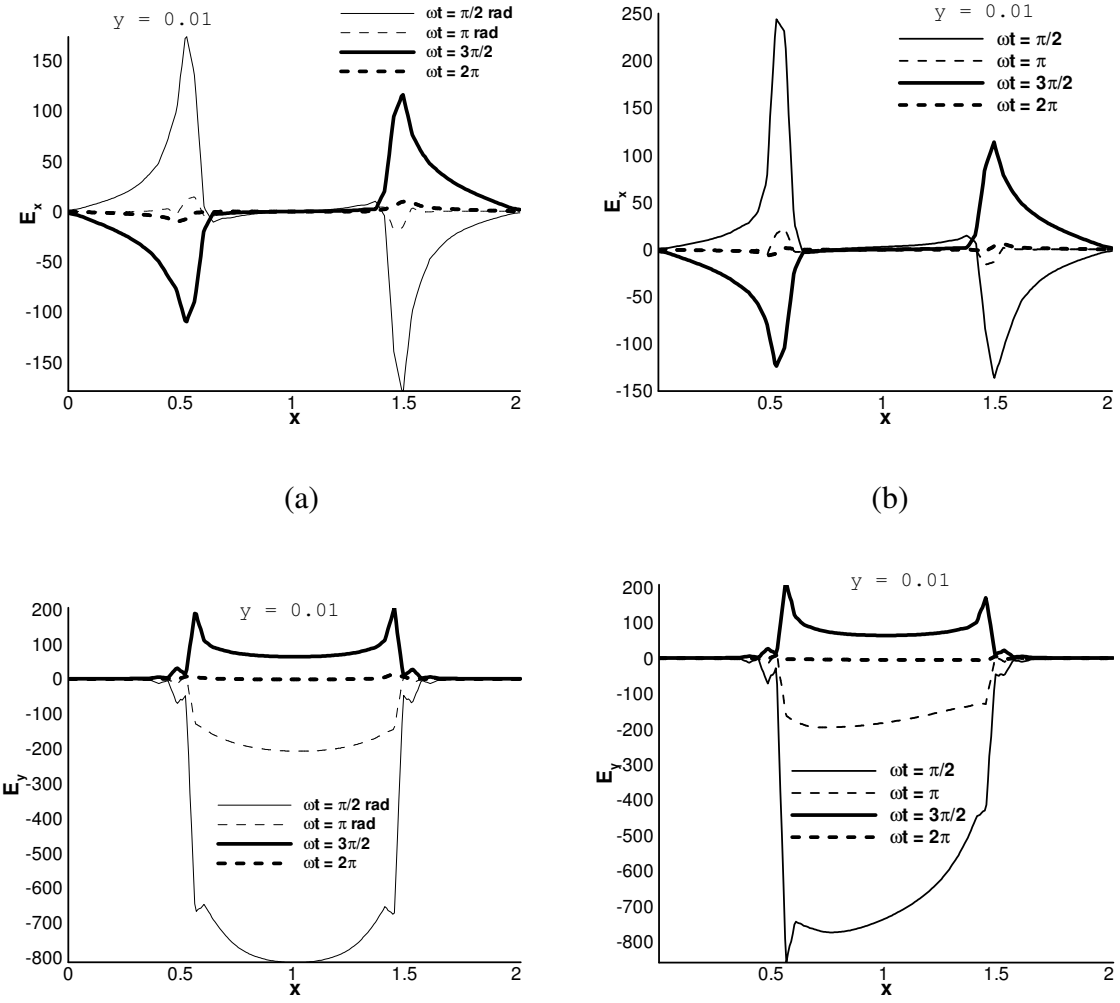

Figure 23. (a) Axial electric field in the absence of magnetic field (b) axial electric field in the presence of 20 Gauss (c) transverse electric field in the absence of magnetic field and (d) transverse electric field in the presence of 20 Gauss at four different times of rf cycle.

The **V×B** coupling also affects the transverse electric field as shown in Figure 23. The effect is more pronounced at $\pi/2$ when the net downward field is predominant in the

near the left insulator-electrode edge. The effect of magnetic field in affecting near wall electrodynamics has been demonstrated here. The local increase or decrease in near wall space charge effect can be related to magnitude and direction of input magnetic field.

Case IV: Edge Effect of Electrodes

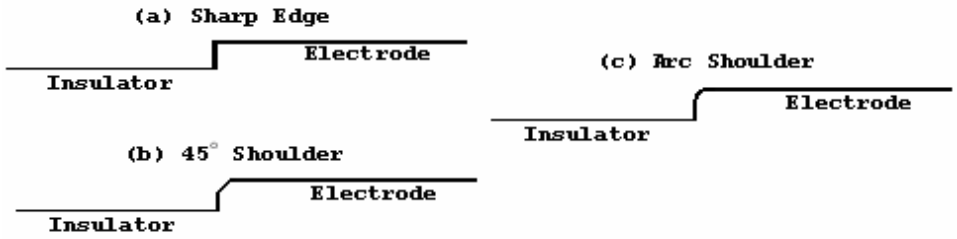

Figure 24. Types of electrode-insulator edge.

It has been demonstrated that the presence of an insulator-conductor interface alters the nature of discharge and plays a significant role in altering electric forces due to plasma generation. The conductor in the previous case was assumed thin for simplicity in modeling. It has been shown recently that the nature of edge between insulator and electrode play a significant role in altering the nature of field lines and hence the "qE" forces near the wall (Enloe, et. al., 2004). To have an insight into this edge effect, two configurations, shown in Figure 24(a) and 24(b) are investigated in the present study. The case of rounded edge (Figure 24(c)) may be visualized as an intermediate case between 90^o and 45^o shoulder configurations.

The present case under consideration is limited to steady state in the absence of magnetic field for simplicity. An electrode of 0.2 mm thickness is coated on a flat plate and located at ~1.5 cm from the left boundary. Figure 24(a) considers a sharp edge of electrode with a 90^o shoulder while Figure 24(b) considers an edge with 45^o chamfer.

The computational grid consists of 45 × 45 bi-quadratic finite elements in both cases. The discharge conditions are same as before, namely, 0.1 torr argon plasma with an electrode potential of –50V.

Figures 23(a) to 23(f) compare the computed profiles for the two electrode edge models under consideration. The region near the edge has been zoomed for clarity. From common understanding, the 90^o edge creates a sharp geometrical discontinuity resulting in abrupt change in radius of curvature across the edge as compared to the bevel. Hence, the spatial variation of electric field gets considerably modified altering the electro-dynamic properties of the discharge between the two edge shapes. The electric field lines for a given change in potential are shown in Figure 23(a) to 23(d) and edge effects are felt within several Debye lengths (~0.1 cm) in the plasma.

Figure 23(e) to 23(f) plots the force vector for the two shapes expressed as a product of space charge difference (N_i-N_e) and electrostatic field, E_x or E_y). In both cases, a strong electrostatic force in the positive *x* and negative *y* direction is noted close to the wall. The presence of cathode gives rise to strong transverse field (with electric field lines ending at cathode perpendicular to it) downstream of the edge. The direction of electric field force vector (given by $\tan^{-1}(F_y/F_x)$) near the wall was predicted between 225^o to 260^o oriented mostly in the third quadrant. This is indicative of an effective forward-downward force created by the plasma across the edge.

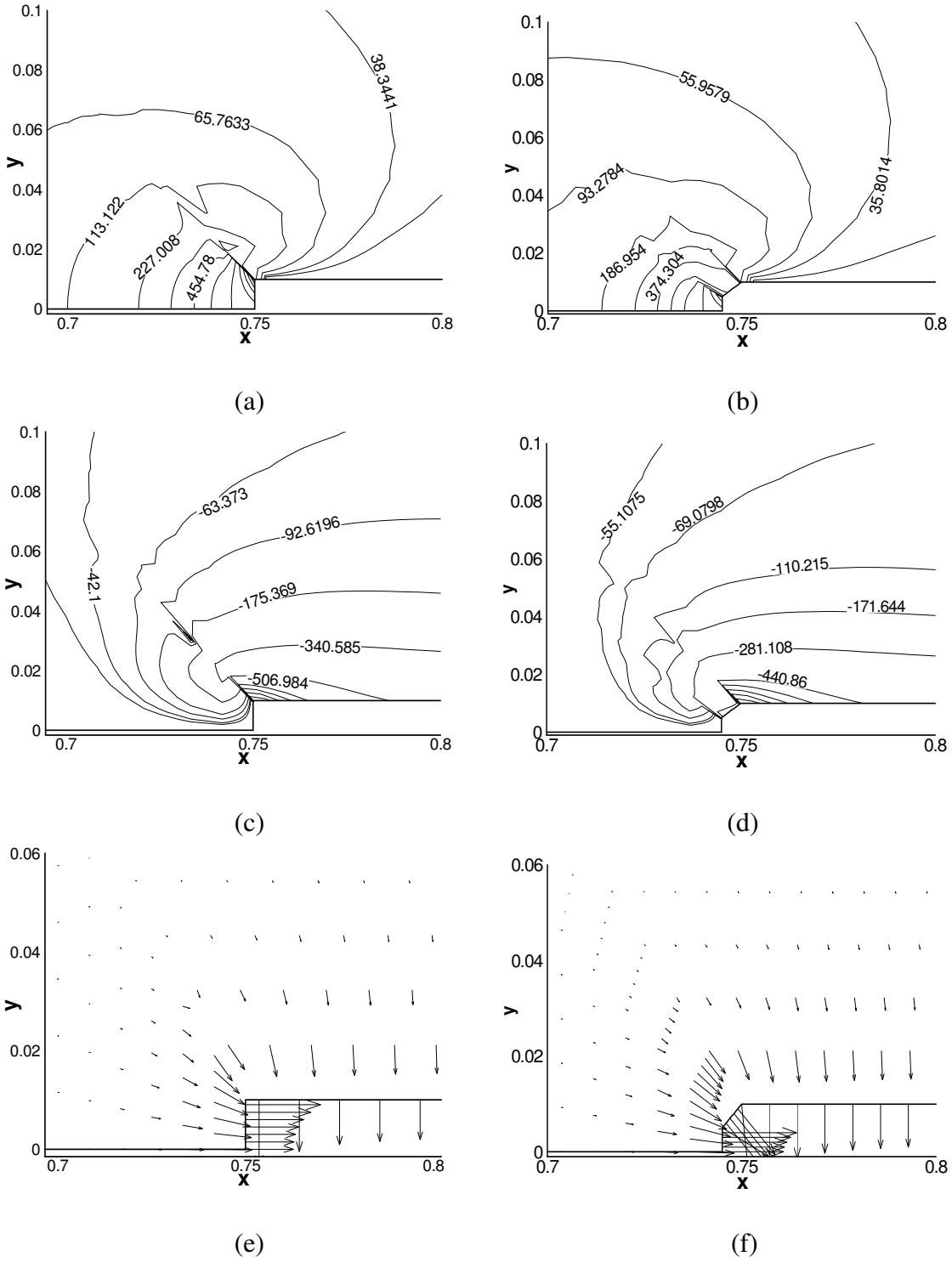

Figure 25. (a) Axial electric field for 90^{o} shoulder (b) axial electric field for 45^{o} shoulder (c) transverse electric field for 90^{o} shoulder (d) transverse electric field for 45^{o} shoulder (e) force vector for 90^{o} shoulder and (e) force vector for 45^{o} shoulder.

V. CONCLUSIONS AND RECOMMENDATIONS

Conclusions

An argon gas discharge under applied rf potential between two electrodes has been modeled from first principles using a self-consistent coupled system of two fluid and a single Poisson equation. The model is based on a robust finite element algorithm utilized to overcome the stiffness of the plasma-wall equations. FE techniques are especially suitable for their adaptability to arbitrary multidimensional geometries and boundary conditions. The high-fidelity finite-element procedure is anchored in a Multiscale Ionized Gas (MIG) flow code. The code allows introduction of element-wise constant and local velocity based artificial diffusion which guarantees a monotone solution and is expected to ensure minimum dispersion error. The details of the algorithm flow of sequence in the code and alterations made to improve computational speed when handling of sparse matrices have been presented. Numerical limitations are highlighted for a simple 1d two fluid formulation from the theoretical derivation of algorithm amplification factor and phase velocity. The intention is to complement experimental efforts by providing a suitable tool to explore flow control concepts in future design and development.

The dynamics of ions and electrons have been reported in one dimensional model for an applied rf frequency $\omega < \omega_{pe}$ and 0.1 torr pressure. The collisional nature of the problem, varying timescales for charged species in the bulk plasma and sheath, and the

use of an interpolation polynomial to simulate the plasma-sheath transition that has abrupt changes in gradients add to the complexity of the problem. The oscillation of the sheath edge has been correlated as a sinusoidal wave. The sheath thickness is of a few Debye lengths and accounts for nearly 80% potential drop for one rf cycle.

The formulation was tested in two-dimension for plasma formed between two symmetric electrodes for a direct current glow discharge using nitrogen. The results match well with published literature. A steady state discharge is simulated for argon in an electrode-insulator configuration. The magnetic field has been shown to strongly affect the stream-wise distribution caused by the $\mathbf{V}\times\mathbf{B}$ coupling between x and y axes. Simulation results for a transient discharge evolution in the presence of time varying rf potential have been investigated. The present analyses have served to highlight the importance of understanding two-dimensional gas discharge nature and the effect of time varying potential and an external magnetic field on it. Finally, the shape effect in insulator-conductor configuration on near wall dynamics is compared using a 90^{o} shoulder and 45^{o} chamfer. The maximum axial force is about ~22% higher for 90^{o} shoulder while the force vector across the edge indicates a net downward and forward force generated.

The potential of combined electric and magnetic fields as a productive means in altering near wall plasma forces has been realized here. The results presented are expected to help interpret the plasma formation in the presence electromagnetic interaction on the discharge structure for higher pressures.

Recommendations

The intent for development of the MIG code for discharge modeling at various pressures is to complement experimental efforts by providing a suitable numerical tool to explore flow control concepts in future design and development. Given the robustness of the algorithm and capability of the code, measures to further improve the computational speed like parallelization are required, particularly for solving unsteady problems. This will possibly cut down simulation time from days to hours. With finite element algorithm (e.g. Galerkin) being increasingly seen as a highly efficient tool for complex flow problems, the code proves as a powerful numerical tool in analysis, design and development.

The simulation of plasma in one-dimension has been done extensively in literature. But exhaustive two-dimensional simulations in the presence of rf interactions and magnetic field are in rudimentary stages. The present formulation is expected to serve as a framework for the following suggested investigations - correlate plasma V-I characteristics for varying magnetic field intensities, rf interactions in presence of magnetic field at high pressures, inclusion of electron temperature equation to study electron heating mechanisms and modeling plasma chemistry for multiple levels of ionization.

REFERENCES

Adamovich, I.V., Subramaniam, V.V., Rich, J.W., and Macheret, S.O. (1998). Phenomenological Analysis of Shock Wave Propagation in Weakly Ionized Plasmas, AIAA Journal, vol. 36(5), pp. 816-822.

Baker, A.J. and Pepper, D.W. (1991). Finite Elements 1-2-3, McGraw Hill, Inc.

Balagangadhar, D. and Roy, S. (2001). Design Sensitivity Analysis and Optimization of Steady Fluid-Thermal Systems Computer Methods in Applied Mechanics and Engineering, vol. 190 (42), pp. 5465-5479.

Boeuf, J. P., (1998). A two-dimensional model of DC glow discharges, Journal of Applied Physics vol. 63(5), pp.1342-1349.

Boeuf, J. P. and Pitchford L. C. (1995). Two-dimensional model of a capacitively coupled rf discharges and comparisons with experiments in the Gaseous Electronics Conference reference reactor, Physical Review E, vol. 51(2), pp.1376-1390.

Bose, D., Govindan, T. R. and Meyyappan, M., (2000). Ion dynamics model for collisionless radio frequency sheaths, Journal of Applied Physics, vol. 87(10), pp. 7176-7184.

Cooper, S.M., Cruden, B., Meyyappan, M., Raju R. and Roy, S. (2004). Gas Transport Characteristics Through a Carbon Nanotubule, Nano Letters, vol. 4(2), pp. 377-381.

Dalvie, M., Surendra, M. and Selwyn, G. S. (1993). Self-consistent fluid modeling of radio frequency discharges in two dimensions, Applied Physics Letters, vol. 62(24), pp. 3207-3209.

Enloe, C. L., McLaughlin, T E., VanDyken, R. D., Kachner, K. D., Eric J. Jumper, Corke, T. C. (2004). Mechanisms and Responses of a Single Dielectric Barrier Plasma Actuator: Plasma Morphology, AIAA Journal vol. 42(3), pp. 589-594.

Fife, J. M. (1995). Two-dimensional hybrid particle-in-cell modeling of Hall thrusters, MS Thesis, Massachusetts Institute of Technology.

Godyak, V., Sternberg, N. (1990). Dynamic model of the electrode sheaths in symmetrically driven RF discharges, Physical Review A vol. 42(4), pp. 2299–2312.

Hagelaar, G. J. M., Bareilles, J., Garrigues, L. and Boeuf, J. P. (2002). Two-dimensional model of a stationary plasma thruster, Journal of Applied Physics, vol. 91(9), pp. 5592-5598.

Hammond, E. P., Mahesh, K. and Moin, P. (2002). A numerical method to simulate radio-frequency plasma discharges, Journal of Computational Physics, vol. 176(2) pp. 402 – 429.

Hou, L-J., Wang, Y-N. and Miskovic, Z. L. (2004). Two-dimensional radio-frequency sheath dynamics over a non-flat electrode with perpendicular magnetic field, Physics of Plasma, vol. 11(9), pp. 4456-4461.

Kaganovich, I. D., Tsendin, L. D. and Yatsenko N. A. (1994). Two-dimensional high-frequency discharge at intermediate pressures, Tech. Physics, 39(12), pp. 1215-1226.

Kim, D. and Economou, D. J. (2003). Simulation of a two-dimensional sheath over a flat wall with an insulator/conductor interface exposed to high density plasma, Journal of applied physics, vol. 94(5), pp. 2852-2857.

Kumar, H. and Roy, S. (2005). Finite element modeling of a two-fluid rf plasma discharge, Third MIT Conference Proceedings, Computational Fluid and Solid Mechanics, Elsevier Science, Paper No. 226-333, pp. 989-992.

Kumar, H. and Roy, S. (2005). Hydrodynamic Model of Plasma-Sheath for rf Discharges with and without Collision, 43rd AIAA Aerospace Sciences Meeting and Exhibit, AIAA-2005-0948.

Kumar, H. and Roy, S. (2005). Multidimensional hydrodynamic plasma-wall model for collisional plasma discharges with and without magnetic field effects, Physics of Plasmas, vol. 12(9), pp. 093508 1-10.

Lieberman, M. and Lichtenberg, A. J. (1994). Principles of plasma discharges and material processing, John Wiley and Sons, Inc.

Miller, P. A. and Riley, M. E. (1997). Dynamics of collisionless rf plasma sheaths, Journal of Applied Physics, vol. 82(8), pp. 3689-3709.

Nitschke, T. E. and Graves, D. B. (1994). A comparison of particle in cell and fluid model simulations of low-pressure radio frequency discharges, Journal of Applied Physics, vol. 76(10), pp. 5646-5660.

Paranjpe, A. P., Mcvittie, J. P. and Self S. A. (1990). Algorithms for numerical simulation of radio-frequency glow discharges, Physical review A, vol. 41(12), pp. 6949-62.

Passchier, J. D. P. and Goedheer, W. J. (1993). A two-dimensional fluid model for an argon rf discharge, Journal of Applied Physics, vol. 74(6), pp. 3744-3751.

Raizer, Y. P., Shneider, M. N. and Yatsenko, N. A. (1995). Radio-frequency capacitive discharges, CRC Press, London.

Richards, A. D., Thompson, B. E. and Sawin, H. H. (1987). Continuum modeling of argon radio frequency glow discharges, Applied physics letters, 50(9), pp. 492-494.

Richtmyer, R.D. and Morton, K.W. (1967). Difference Methods for Initial-Problems, 2nd Ed, Interscience Publishers, Wiley, New York.

Roth, J. R. (2003). Aerodynamic flow acceleration using paraelectric and peristaltic electro hydrodynamic effects of a One Atmosphere Uniform Glow Discharge Plasma, Physics of Plasmas, vol. 10(5), pp. 2117.

Roy Choudhuri, A. (1998). Physics of Fluids and Plasmas: An Introduction for Astrophysicists, Cambridge University Press.

Roy, S., Pandey, B. P., Poggie, J. and Gaitonde D. (2003). Modeling low pressure collisional plasma sheath with space-charge effect, Physics of Plasmas, vol. 10(6), pp. 2578-2585.

Roy, S. (1994). On Improved Methods for Monotone CFD Solution Accuracy, University of Tennessee, Knoxville, pp. 1-395.

Roy, S. and Baker, A. J. (1998). Sub Grid embedding (SGM) Algorithm - Part II, Navier-Stokes solutions, Journal of Numerical heat transfer, vol. 33(1), pp. 5-36.

Roy, S. and Gaitonde, D. (2004). Radio frequency induced ionized collisional flow model for application at atmospheric pressures, Journal of Applied Physics, vol. 96(5), pp. 2476-2481.

Roy, S. and Pandey, B.P. (2002). Numerical Investigation of a Hall Thruster Plasma, Physics of Plasmas, vol. 9(9), pp. 4052-60.

Roy, S. (2005). Flow actuation using radio frequency in partially-ionized collisional plasmas, Applied Physics Letters, vol. 86(10), pp. 101502:1-3.

Slemrod, M. (2003). The Radio-Frequency Driven Plasma Sheath: Asymptotics and Analysis, SIAM Journal of Applied Math., vol. 63(5), pp. 1737.

Sternberg, N. and Godyak, V. A. (1996). Approximation of the bounded plasma problem by plasma and sheath models, Physica D vol. 97, pp. 498-508.

Sternberg, N. and Godyak V. A. (2003). On Asymptotic Matching and the Sheath Edge, IEEE Transactions On Plasma Science, vol. 31 (4), pp. 665-677.

Surzhikov, S. T. and Shang, J. S. (2004). Two-component plasma model for two-dimensional glow discharge in magnetic field, Journal of Computational Physics, vol.199(2), pp. 437-464.

Ward, L. (1962). Calculation of cathode-fall characteristics, Journal of Applied Physics, vol. 33(9), pp. 2789-2794.

Wanless, D. (1971). Electron-ion recombination in argon, J. Phys. B: Atom. Molec. Phys., Vol. 4, pp. 522-527.

Xiang, N. and Waelbroeck, F. L. (2003). Effects of presheath dynamics on radio-frequency sheaths, vol. 93(9) pp. 5034-5042.

Zhang, Y., Liu, J., Liu, Y. and Wang X. (2004). Characteristics of a plasma sheath in radio frequency biased voltage Physics of Plasmas, vol. 11(8), pp. 3840.

NOMENCLATURE

t	Time co-ordinate, s
x, y	Spatial co-ordinates, cm
λ_D	Debye length, cm
T	Temperature, K
k	Boltzman constant, J/K
e	Elementary charge, coulomb
N	Number density, cm^{-3}
V	Species hydrodynamic velocity, cm/s
M,m	Mass of charged species, Kg
P	Pressure
ν	Frequency, s^{-1}
E	Electric field, V/cm
φ	Potential, V
ε	Permittivity, $C^2/N.m^2$
f	Applied frequency, Hertz
ω	Applied frequency, s^{-1}
d	Characteristic length, cm
α	Ionization coefficient, cm^{-1}
β	Recombination coefficient
L	Linear operator
q	State variable
w	Weight function
f	Flux vector
Ω	Computational domain
η	Artificial diffusion parameter

G	Amplification parameter
Φ	Phase velocity
Δ	Increment
C	Courant number
ψ	Test function
F, R	Residual
Γ	Flux, cm^{-2}/s
μ	Mobility, $cm^2V^{-1}s^{-1}$
D	Diffusion coefficient, cm^2/s
I	Current
A, B	Constants
B_z	Magnetic field, Tesla
J	Jacobian
∇	Gradient

Subscripts:

e	Electron
i	Ion
n	Neutral
B	Bohm
0	Reference value

APPENDICES

APPENDIX A

FORTRAN 77 SUBROUTINE FOR ALTERNATE FINITE ELEMENT ASSEMBLY METHOD

```
c This subroutine assembles the element matrix contributions to global matrix

Subroutine assemgm (elemk, ndim, maxdim, elemdof, iwant, iel, mtemp, ktemp)

c  elemk          - element stiffness matrix
c ktemp,mtemp     - local element and mass matrices
c  maxdim         - leading dimension of elemk
c  ndim           - order of elemk
c  elemdof        - element d-o-f array
c dof_node        - number of degree of freedom in a node
c ielx            - number of elements in x direction in the model
c irow            - row index
c icol            - column index

      implicit none
      include 'common_include'
      integer iwant
      integer ndim, maxdim,ndof,iel,ielx, dof_node, domain
      parameter (ielx = 20)
      parameter(dof_node=3)
      parameter(domain = 4*dof_node)
      real*8 elemk(maxdim, *), ktemp(maxdim, *), mtemp(maxdim, *)
      integer elemdof(*)
      integer irow, icol, i, j, k, count, itest, ii, jj
      integer locate(domain+1,domain+1,2*ielx+1), iel_num, iel_store
      integer bottom, left, m, n, set

c Initialize location flags
       left = 0
       bottom = 0

c Store location flags
        if(iel.gt.ielx.and.mod(iel-1,ielx).eq.0) left = 1
        if(iel.le.ielx) bottom = 1

c Initialize to 0 for every new iteration
       itest = 0
      if(iel.eq.1.and.count.ne.1) then
        nelt = 0
           do i=1,domain+1
            do j=1,domain+1
             do k=1,2*ielx+1
              locate(i,j,k)=0
             enddo
            enddo
           enddo
        count = 1
```

```
      endif
      if(iel.ge.2) count = 0

      iF (.not. steady) then
          if(iwant.eq.2) itest = 1
      Else
          if(iwant.eq.3) itest = 1
      Endif

c  Alter element number suitably
        iel_num = mod(iel,2*ielx)
        if(iel_num.eq.0) iel_num = 2*ielx

        if(iel_num.gt.ielx) iel_store = iel_num - ielx
        if(iel_num.le.ielx) iel_store = iel_num + ielx

        if(iel.le.ielx) iel_store = iel

c Outer element information scanning loop begins
      do 10 i = 1, ndim

        irow = elemdof(i)

      do 20 j = 1, ndim

          icol = elemdof(j)

c Skip negative index
         if(irow.lt.0.or.icol.lt.0)  goto 130

c Depending on row and column number, add to appropriate matrix

          IF (iwant.eq.0.or.iwant.eq.3) THEN

           if(.not.steady) then
            ktemp(i,j)= elemk(i,j)*delta_time*wilson_theta
           else
            ktemp(i,j) = elemk(i,j)
           endif


          ENDIF

          IF(itest.eq.1) THEN

          ktemp(i,j) =  mtemp(i,j) + ktemp(i,j)
```

```
      if(iel.eq.1) then
        if(ktemp(i,j).ne.0.d0) then
         nelt = nelt + 1
         a(nelt) = ktemp(i,j)
         ipos(nelt) = irow
         jpos(nelt) = icol
         locate(i,j,1) = nelt
       else
         locate(i,j,1) = 0
       endif
     endif

      IF(iel.gt.1) THEN

c Retrieving information from locate for shared nodes
c For node 1-1 contribution of present element to appropriate location
        if(i.ge.1.and.i.le.dof_node) then
        if(j.ge.1.and.j.le.dof_node) then

            if(left.eq.1)  ii = locate(i+3*dof_node,j+3*dof_node,iel_store)

            if(bottom.eq.1)
     &       ii = locate (i+dof_node,j+dof_node,iel_store-1)

            if(left.ne.1.and.bottom.ne.1)
     &       ii = locate (i+2*dof_node,j+2*dof_node,iel_store-1)

            if(ii.gt.0)   a(ii) = a(ii) + ktemp(i,j)
            goto 120
         endif
        endif

      IF(left.ne.1) THEN
c Add node 4-1 contribution of current element
        if(i.ge.1+3*dof_node.and.i.le.4*dof_node) then
        if(j.ge.1.and.j.le.dof_node) then
             ii = locate(i-dof_node,j+dof_node,iel_num-1)
             if(ii.gt.0)  a(ii) = a(ii) + ktemp(i,j)
             goto 120
        endif
        endif

c Similar loop for node 1-4

c Add node 4-4 contribution of current element
```

```
        if(i.ge.1+3*dof_node.and.i.le.4*dof_node) then
        if(j.ge.1+3*dof_node.and.j.le.4*dof_node) then
            ii = locate(i-dof_node,j-dof_node,iel_num-1)
            if(ii.gt.0) then
              a(ii) = a(ii) + ktemp(i,j)
            else
              if(ktemp(i,j).ne.0.d0) then
               nelt = nelt + 1
               a(nelt) = ktemp(i,j)
               ipos(nelt) = irow
               jpos(nelt) = icol
               m=i-dof_node
               n=j-dof_node
               locate(m,n,iel_num-1) = nelt
              endif
            endif
           goto 120
        endif
        endif

      ENDIF

      IF(bottom.ne.1) THEN

c Add node 2-1 contribution of current element
        if(i.ge.1+dof_node.and.i.le.2*dof_node) then
        if(j.ge.1.and.j.le.dof_node) then
            ii = locate(i+dof_node,j+3*dof_node,iel_store)
            if(ii.gt.0)
     &          a(ii) = a(ii) + ktemp(i,j)
              goto 120
        endif
        endif

c Similar loop for node 1-2

c Node 2-2
        if(i.ge.1+dof_node.and.i.le.2*dof_node) then
        if(j.ge.1+dof_node.and.j.le.2*dof_node) then
            ii = locate(i+dof_node, j+dof_node, iel_store)
            if(ii.gt.0) then
              a(ii) = a(ii) + ktemp(i,j)
            else
              if(ktemp(i,j).ne.0.d0) then
               nelt = nelt + 1
               a(nelt) = ktemp(i,j)
```

```
            ipos(nelt) = irow
            jpos(nelt) = icol
            m=i+dof_node
            n=j+dof_node
            locate(m,n,iel_store) = nelt
           endif
         endif
        goto 120
      endif
      endif

     ENDIF

c Storage of new entry into locate matrix

      if(ktemp(i,j).ne.0.d0) then
         nelt = nelt + 1
         a(nelt) = ktemp(i,j)
         ipos(nelt) = irow
         jpos(nelt) = icol
         locate(i,j,iel_num) = nelt
      else
         locate(i,j,iel_num) = 0
      endif

      ENDIF

 120  continue_flag = 1
      endif
 130  continue_flag = 1

 20   continue
 10   continue

      return
      end
```

APPENDIX B

FORTRAN 77 SUBROUTINE FOR ELEMENT MATRIX FORMATION

```
      subroutine FEelement (elemk, elemf, elemutminus, elemutplus, elemx, elemmatprop,
     &                      max_elem_dim, max_dim, eltype, iwant, nelems, iel)

c "FEelement" is an element subroutine for a bi-quadratic element containing all
c information required to form a element matrix

c  elemdim        - Dimension of the element matrix (degrees of freedom of an element)
c  loc_<var>      - Location of variable name <var> in the element matrix
c  Nmat,DNmat     - Basis function and derivative
c elemx           - x and y location of a node in an element of the domain
c  elemk          - Element stiffness matrix

c  Algorithm-specific variable and constant-declaration

      implicit none
      integer max_elem_dim, max_dim, eltype, iwant, elemdim, nelems, iel
      real*8 elemk(max_elem_dim,*), elemf(*), elemutminus(*), elemutplus(*)
      real*8 elemx(max_dim,*), elemmatprop(*)

      parameter (elemdim = 27)
      integer nint, iint, i, j, ii, jj
      integer loc_Ni(9), loc_Ne(9), loc_phi(9),
      real*8 rint(9), wint(9), sint(9), jac, rr, wt, ss
      real*8 Nmat33(9), DNmat33Dx(9), DNmat33Dy(9)
      real*8 elemk_lin(elemdim,elemdim), elemk_non_lin(elemdim,elemdim)
      real*8 term, constant

c  Problem-specific variables and constants - declaration

      real*8 Ne, DNeDx, DNeDy, Ni, DNiDx, DNiDy, phi, DphiDx, DphiDy
      real*8 nevex, nevey, neve, Ex, Ey, E
      real*8 mewi, mewe, t_0, kb, p_l, pi, omega, new
      real*8 epsilon, N_0, eps, mi, vb, me
      real*8 mag, omi, ome, alpha, e_charge, p, Te, Di, De, A, B

c Control variables
      loc_Ni(1) = 1
      loc_Ni(2) = 4
      loc_Ni(3) = 7
      loc_Ni(4) = 10
      loc_Ni(5) = 13
      loc_Ni(6) = 16
      loc_Ni(7) = 19
      loc_Ni(8) = 22
      loc_Ni(9) = 25
```

```
      do i = 1,9
       loc_Ne(i)   =  loc_Ni(i) + 1
       loc_phi(i)  =  loc_Ni(i) + 2
      enddo

c Electron , ion  parameters and ionization rate

c    e_charge  is  charge of electron
c     p  is  pressure in torr
c     Te  is  temperature of electron
c     Ti  is  temperature of ion
c     Di  is  ion diffusion coefficient
c     De  is  electron diffusion coefficient
c     p_l  is  characteristic plasma length
c    omega  is  applied rf biased frequency
c     kb  is  boltzman constant
c     mi  is  mass of ion
c     mag is the magnetic field

       kb = 1.3807* 1.e-23
       p = 0.1
       epsilon = 8.8532 * 1.e-12
       e_charge = 1.6022 * 1.e-19
       pi = 3.14159
       Te = 11600.d0
       omega = 13.56* 1.e6 * 2.d0 * 3.14159
       mi   = 40.d0 * 1.6726 * 1.e-27
       me = 9.1038 * 1.e-31
       vb   = dsqrt(Te * kb / mi)

c Non-dimensional variables

       p_l = 0.02
       t_0 = 1.0 / omega
       n_0 = 2.e15
       alpha =  p_l/(vb*t_0)
       eps = epsilon*kb*Te/(e_charge**2 * n_0 * p_l**2)

       mewe = 3.0*1.e5 / p * 1.e-4

       mag = 0.002
       omi = 1.d0
       ome = 1.d0 + mewe**2 * mag**2


      call zero (elemk_lin,elemdim,elemdim,elemdim)
```

```
      call zero (elemk_non_lin,elemdim,elemdim,elemdim)
      call zero (elemk,elemdim,elemdim,max_elem_dim)
      call zero (elemf,elemdim,1,max_elem_dim)

      call setup_integration (rint,wint,nint,3)
      call integ_pt_1t2d (rint,sint,wint,nint)

      do iint = 1, nint
        rr = rint(iint)
        ss = sint(iint)

        call shape_fn_2d_3x3(Nmat33, DNmat33Dx, DNmat33Dy, jac, rr, ss, elemx,
        max_dim)

        Ni = 0.d0
        DNiDx = 0.d0
        DNiDy = 0.d0

        Ne = 0.d0
        DNeDx = 0.d0
        DNeDy = 0.d0

        phi = 0.d0
        DphiDx = 0.d0
        DphiDy = 0.d0

c Cell averaged values

        do i = 1,9
          ii = loc_Ni(i)
          Ni = Ni + Nmat33(i) * elemutplus(ii)
          DNiDx = DNiDx + DNmat33Dx(i) * elemutplus(ii)
          DNiDy = DNiDy + DNmat33Dy(i) * elemutplus(ii)

          ii = loc_Ne(i)
          Ne = Ne + Nmat33(i) * dabs(elemutplus(ii)
          DNeDx = DNeDx + DNmat33Dx(i) * elemutplus(ii)
          DNeDy = DNeDy + DNmat33Dy(i) * elemutplus(ii)

          ii = loc_phi(i)
          phi = phi + Nmat33(i) * elemutplus(ii)
          DphiDx = DphiDx + DNmat33Dx(i) * elemutplus(ii)
          DphiDy = DphiDy + DNmat33Dy(i) * elemutplus(ii)
        enddo

        Ex = -DphiDx
```

```
      Ey = -DphiDy
      E  = (Ex**2 + Ey**2)**0.5
      nevex = (-Ne*mewe*1.e4* Ex - mewe*1.e4 * DNeDx )/(p_l*100.0)
      nevey = (-Ne*mewe*1.e4* Ey - mewe*1.e4 * DNeDy )/(p_l*100.0)
      neve = (nevex**2 + nevey**2)**0.5

c Ionization rate

        A = 34.0
        B = 16.0
        new = [A *p *dexp(-B/(E/p)) * neve ] * p_l / vb

c Ion mobility calculation

        Ex = -(elemutminus(loc_phi(2))-elemutminus(loc_phi(1)))/
     &                    (elemx(1,2)-elemx(1,1)) / (p_l*100.0)
        Ey = -(elemutminus(loc_phi(4))-elemutminus(loc_phi(1)))/
     &                    (elemx(2,4)-elemx(2,1)) / (p_l*100.0)
        E  = (Ex**2 + Ey**2)**0.5

      if( (E/p).le.60.d0 ) then
        mewi = 1.e3 * (1.d0 - 2.22e-3 * E/p) * 1.e-4 / p
      else
        mewi = 8.25e3/dsqrt(E/p) * 1.e-4 / p
      endif

c Non-dimensional local electric field in an element

        Ex = -(elemutminus(loc_phi(2))-elemutminus(loc_phi(1)))/
     &                    (elemx(1,2)-elemx(1,1)) / p_l
        Ey = -(elemutminus(loc_phi(4))-elemutminus(loc_phi(1)))/
     &                    (elemx(2,4)-elemx(2,1)) / p_l

      wt = wint(iint) * jac

      IF (iwant.eq.0) then

c Integration of spatial terms

    do i = 1,9

        ii = loc_Ni(i)
        elemf(ii) = elemf(ii) -wt * new * Nmat33(i)

        ii = loc_Ne(i)
        elemf(ii) = elemf(ii) - wt * new * Nmat33(i)
```

```
      do j = 1,9

c############## Equation for Ni ###############
            ii = loc_Ni(i)

c for dphi/dx Ni
            jj = loc_Ni(j)
            term=  wt * mewi/(p_l*vb) * Nmat33(i) *DNmat33Dx(j)*
     &          ( (-DphiDx) + mewi*mag*(-DphiDy) )
            elemk_lin(ii,jj) = elemk_lin(ii,jj) + term

c for -d2Ni/dx2
            jj = loc_Ni(j)
            term= wt * Di * DNmat33Dx(i) * DNmat33Dx(j)
            elemk_lin(ii,jj) = elemk_lin(ii,jj) + term

c for - d2Ni/dy2
            jj = loc_Ni(j)
            term= wt * Di *  DNmat33Dy(i) * DNmat33Dy(j)
            elemk_lin(ii,jj) = elemk_lin(ii,jj) + term

c for dphi/dy Ni
            jj = loc_Ni(j)
            term=  wt * mewi/(p_l*vb)
     &             * Nmat33(i) *DNmat33Dy(j)*
     &          ( (-DphiDy) - mewi*mag*(-DphiDx) )
            elemk_lin(ii,jj) = elemk_lin(ii,jj) + term

c for +Ni*(Ni-Ne)/eps
            jj = loc_Ni(j)
            term=  wt * mewi/(p_l*vb)
     &              * Nmat33(i) *Nmat33(j) * (Ni-Ne)/eps
            elemk_lin(ii,jj) = elemk_lin(ii,jj) + term

c Similar formulation for Ne

c############## Equation for Phi ###################
            ii = loc_phi(i)

c   (eps) d2ϕ/dx2
            jj = loc_phi(j)
            term = -wt * eps*
     &              (  DNmat33Dx(i) * DNmat33Dx(j)
     &              +  DNmat33Dy(i) * DNmat33Dy(j) )
            elemk_lin(ii,jj) = elemk_lin(ii,jj) + term
```

```
c   -Ne
          jj = loc_Ne(j)
          elemk_lin(ii,jj) = elemk_lin(ii,jj) -wt * Nmat33(i) * Nmat33(j)

c   +Ni
          jj = loc_Ni(j)
          elemk_lin(ii,jj) = elemk_lin(ii,jj) + wt * Nmat33(i) * Nmat33(j)

c End of loop for elemk formation from spatial terms

          enddo
          enddo

        ENDIF

c Integration of time terms

       IF (iwant.eq.1) then

         do i = 1,9
         do j = 1,9

c +alpha * dNi/dt
            ii = loc_Ni(i)
            jj = loc_Ni(j)
            elemk(ii,jj) = elemk(ii,jj) +  wt * alpha * Nmat33(i) * Nmat33(j)

c +alpha * dNe/dt
            ii = loc_Ne(i)
            jj = loc_Ne(j)
            elemk(ii,jj) = elemk(ii,jj) +  wt * alpha * Nmat33(i) * Nmat33(j)

          enddo
          enddo

       ENDIF

c End of integration loop
      enddo

c Global matrix formation

      IF (iwant.eq.0) then

       do i = 1,elemdim
       do j = 1,elemdim
```

```
          elemk(i,j) = elemk_lin(i,j) + elemk_non_lin(i,j)
          elemf(i) = elemf(i) + elemk(i,j) * elemutplus(j)
        enddo
        enddo

      ENDIF

c Negative force for the N.R. Scheme

      do i = 1, elemdim
       elemf(i) = - elemf(i)
      enddo
      return
      end
```